Swimming *Euglena* respond to confinement with a behavioral change enabling effective crawling

Giovanni Noselli[1], Alfred Beran[2], Marino Arroyo[*3,4], and Antonio DeSimone[*1,5]

[1]*SISSA–International School for Advanced Studies, 34136 Trieste, Italy*
[2]*OGS–Istituto Nazionale di Oceanografia e di Geofisica Sperimentale, 34151 Trieste, Italy*
[3]*Universitat Politècnica de Catalunya-BarcelonaTech, 08034 Barcelona, Spain*
[4]*Institute for Bioengineering of Catalonia (IBEC), The Barcelona Institute of Science and Technology, 08028 Barcelona, Spain*
[5]*The BioRobotics Institute, Scuola Superiore Sant'Anna, 56127 Pisa, Italy*

Abstract

Some euglenids, a family of aquatic unicellular organisms, can develop highly concerted, large amplitude peristaltic body deformations. This remarkable behavior has been known for centuries. Yet, its function remains controversial, and is even viewed as a functionless ancestral vestige. Here, by examining swimming *Euglena gracilis* in environments of controlled crowding and geometry, we show that this behavior is triggered by confinement. Under these conditions, it allows cells to switch from unviable flagellar swimming to a new and highly robust mode of fast crawling, which can deal with extreme geometric confinement and turn both frictional and hydraulic resistance into propulsive forces. To understand how a single cell can control such an adaptable and robust mode of locomotion, we developed a computational model of the motile apparatus of *Euglena* cells consisting of an active striated cell envelope. Our modeling shows that gait adaptability does not require specific mechanosensitive feedback but instead can be explained by the mechanical self-regulation of an elastic and extended motor system. Our study thus identifies a locomotory function and the operating principles of the adaptable peristaltic body deformation of *Euglena* cells.
max length in this format: 8,5 pages + figures

---

[*]Corresponding authors
marino.arroyo@upc.edu
desimone@sissa.it

Euglenids are a diversified family of unicellular flagellated protists abundant in a variety of aquatic ecosystems. Many species of euglenids are capable of performing large amplitude, elegantly coordinated cell body deformations. This behavior is referred to as the euglenoid movement or *metaboly*.[1,2,3] Depending on the species and within a species, metaboly can range from rounding and gentle bending or twisting to periodic highly concerted peristaltic waves traveling along the cell body. Observations of metaboly date back to the first microscopists,[4] and have fascinated researchers across disciplines ever since. It is known that an active striated cell envelope, called pellicle, controls cell shape.[1,5,6,7] However, the precise mechanism by which this cortical complex performs metaboly, including the molecular motors involved, is not known. More strikingly, the function of this behavior remains elusive.

Metaboly has been interpreted as a mode of locomotion in a fluid environment.[8] In fact, the peristaltic version of metaboly has inspired prototypical models for low Reynolds number swimming,[9] and theoretical studies have shown that, thanks to its non-reciprocal nature, it is a competent swimming strategy.[7] Yet, since euglenids exhibiting metaboly are also capable of flagellar locomotion,[10] which allows them to move in a fluid about 50 times faster, swimming is not a compelling function justifying metaboly, a behavior requiring an extended and intricate cellular machinery.[1,2,3] In euglenids feeding on large eukaryotic cells, it is accepted that metaboly enables the large cell deformations required for phagocytosis. Since eukaryovorous ancestors have evolved into osmotrophic and autotrophic euglenids, which do not engulf large particles but still exhibit metaboly, it has been argued that metaboly in these species may be an ancestral vestige without a specific function.[11,12,13] It has also been speculated that metaboly may be useful to break the protective cyst that some species can secrete and exit from it, to move in confined environments when some species penetrate dead animals or eggs to feed, or when other species lacking emergent flagella crawl in granular media.[1,14] These hypotheses, however, have not been systematically examined.

Confinement triggers metaboly

To investigate the role of confinement in the behavior of euglenids and their motility, we examined cultures of *Euglena gracilis*, a prototypical photosynthetic species exhibiting metaboly, at various degrees of crowding (Fig. 1a and Supplementary Movie S1). In dilute cultures, cells exhibited fast swimming in the posterior-to-anterior direction powered by an anterior flagellum, cruising at $\sim 68\,\mu\text{m/s}$. During flagellar swimming, cells maintained a fixed cigar shape $\sim 50\,\mu\text{m}$ long and with a maximum diameter of $\sim 9\,\mu\text{m}$. Cells performed sharp turns as previously described.[15] In crowded cultures, presumably triggered by mechanosensation at the cell envelope and/or at the flagella,[1] cells exhibited a variety of behaviors in addition to fast swimming, including rounding, bulging, and large amplitude periodic cell deformations. Rounding was often associated with cell spinning, whereas metaboly did not seem to have a significant effect in locomotion.

We also triggered metaboly by confining cells between two glass plates separated along one side by a spacer to produce a wedge-shaped fluid chamber. Cells in the narrower regions of the chamber (with a typical gap of $\sim 5\,\mu\text{m}$) systematically developed large amplitude periodic shape changes. Using brightfield reflected light microscopy (Supplementary Methods), we were able to record simultaneously and continuously in time the shape changes and the reconfigurations of the pellicle envelope in the plane of the glass plate (Fig. 1b and Supplementary Movies S2 and S3). The pellicle is composed of interlocking narrow and long proteinaceous strips, often arranged helically and spanning from the anterior to the posterior ends of the cell. These strips lie beneath the plasma membrane and are subtended by systems of microtubules.[2] Previous observations in another species (*Euglena fusca*) showed that cell deformations were accompanied by sliding between adjacent pellicular strips, which kept constant their length and width,[1,5,16] similarly to how flagellar shape depends on microtubule sliding in the axoneme.[17] Inter-strip active sliding results in local deformation of the cell envelope, a simple shear along the direction of the strips (Fig. 1c), which when coordinated in space and time can explain the shape dynamics during metaboly.[7,18]

Our continuous observations were consistent with this sliding model; strip width remained nearly constant ($\sim 560\,\text{nm}$), and in agreement with a simple shear local deformation of the pellicle, the total cell area remained nearly constant during shape transformations (Supplementary Methods). To further examine the

shape-morphing mechanism, we developed a theoretical model linking strip curvature on a planar surface, as in Fig. 1(b), and differential sliding along this strip, Fig. 1(d) and Supplementary Note 1. It allowed us to quantify over time the sliding displacement along selected strips, Fig. 1(e), finding net sliding inter-strip displacements of about one micron during the shape excursion in Fig. 1(b). By comparing sliding displacements at different instants, we estimated sliding velocities of up to ∼ 1 µm/s, compatible with those of molecular motors along microtubules.[19] Besides confirming the pellicle strip sliding model, these observations showed that cell volume was nearly constant during metaboly (Supplementary Methods). Interestingly, cells performing metaboly confined between two parallel plates exhibited directed motion in the anterior-to-posterior direction at speeds ranging between 0.08 and 0.2 body lengths per cycle (Supplementary Movies S2 and S3).

To mimic the more realistic situation of multidimensional confinement while having a high degree of experimental control, we drove swimming cells towards tapered glass capillaries with diameter ranging between 300 µm and 6 µm with slopes always smaller than 0.006 in the region of interest, Fig. 1(f) and Supplementary Fig. 2. When the diameter of the capillary was significantly larger than the cell diameter, cells exhibited fast swimming. As cells moved towards the narrow end of the capillary, they collided with the wall and started developing the behaviors described in the crowded cultures, including bulging and rounding, Supplementary Movie S4. By rounding, some cells were able to switch their orientation in the capillary, Supplementary Movies S4 and S5. Most cells eventually developed characteristic highly coordinated and periodic peristaltic body deformations consisting of a bulge moving in the posterior-to-anterior direction followed by a recovery phase during which the bulge at the posterior end reappears at the expense of that at the anterior end, Fig. 1(f)iv and Supplementary Movie S4. Thus, similarly to culture crowding, confinement provided by the capillary triggered changes in cell behavior, which now seemed to acquire a function: cell rounding to turn and metaboly to crawl.

Metaboly is an effective crawling strategy

Close examination of cells performing metaboly in the capillary showed that during their gait, the bulge moving in the posterior-to-anterior direction transiently contacted the capillary wall propelling the cell in the anterior-to-posterior direction, opposite to that of flagellar swimming, Fig. 2(a)i and Supplementary Movie S6. The kinematics of the gait were highly non-reciprocal, and thus in principle compatible with self-propulsion in the non-inertial limit of our experiments.[20] Since cells could switch direction in the capillary, we observed cells crawling by metaboly away from and towards its narrower end. As a result, we were able to examine the features of this mode of locomotion at varying degrees of confinement. To ease understanding of pellicle kinematics, we arranged images in the figures and movies so that cells crawl from left to right. At higher confinement, cells adapted their gait by developing a broader bulge, which remained in contact with the wall during a larger fraction of the gait, Fig. 2(a)ii and Supplementary Movie S6. However, the essential features of the crawling mechanism remained the same.

Kymographs of cells crawling showed the high regularity of the gait and its adaptation to increasing confinement, Fig. 2(b). They also revealed that the net cell displacement was the result of a power phase, when the bulge travels towards the anterior end, and a recovery phase with backward cell motion. Remarkably, cells were able to crawl up to very high degrees of confinement, despite the little space available for shape transformations. Cells crawled fastest, at about 2.5 µm/s (0.4 body lengths per cycle), at intermediate degrees of confinement, where the bulge established sustained contact with the capillary walls and there was sufficient space for significant shape excursions, Fig. 2(c). The period of the gait, however, was largely independent of confinement, Fig. 2(d). Interestingly, the very small crawling velocities we recorded for weakly confined cells (Fig. 2(a) and largest diameter in Fig. 2(c)), which represent a transition between crawling and swimming, are in agreement with a theoretical study examining the complementary situation of swimmers undergoing large shape changes near walls under weaker capillary confinement.[21]

We then wondered if flagellar locomotion of fixed-shape cells would be effective in this situation. Confined cells propelled by flagella would have to overcome a frictional force against the capillary walls and a hydraulic resistance. We theoretically estimated that such cells would move 10 to 20 times slower than those

3

97 crawling by metaboly, Supplementary Note 3. These estimations were consistent with observations of stuck
98 cells beating their flagella, Supplementary Movie S8. Thus, by developing metaboly under confinement,
99 cells switched from ineffective flagellar propulsion to a highly robust crawling mode of locomotion.

Mechanism for locomotion during metaboly

101 To propel their body forward during migration in a low Reynolds number limit, *Euglena* cells must exert self-
102 equilibrated forces on their environment, here, the walls and the fluid within the capillary. To experimentally
103 characterize the physical interaction between cells and their environment, we drove cells not exhibiting
104 deformations into narrow sections of capillaries by applying a known pressure difference while recording
105 cell velocity, contact area, and motion of suspended beads, Supplementary Movie S7. These observations
106 established that confined cells acted as hydraulic plugs and characterized the friction between cells and the
107 wall as viscous and confinement-dependent, Supplementary Note 2.

108   We attempted to understand force transmission during crawling by metaboly in the light of a prevalent
109 model of animal cells crawling in narrow spaces. According to this model, non-adherent confined cells
110 generate propulsive forces through retrograde actin flows and unspecific friction with the confining wall.
111 This propulsive force is balanced by a resistive hydrodynamic force required to displace the water column
112 in the capillary,[22,23,24,25,26] unless water transport is sufficiently fast across the cell.[27] This framework has
113 explained why a large hydraulic resistance relative to the wall friction stalls cell motion and results in
114 fast retrograde flow, whereas vanishing hydraulic resistance leads to fast cell motion and minimal sliding
115 between the polarized actin cytoskeleton relative to the wall. Transposing this model to *Euglena* cells
116 crawling by metaboly, the backward motion of the pellicle bulge would be the analog of retrograde actin
117 flow of animal cells, Fig. 3(a).

118   To test this analogy, we developed an idealized theoretical model of the power phase of the gait con-
119 sistent with the shape-morphing principle of the pellicle of euglenids,[7,18] Fig. 3(b). In this model, a bulge
120 establishes contact with a capillary of radius r over a length ℓ_c, and moves backwards at speed $c < 0$ in
121 the reference frame of the cell, which otherwise is a cylinder of radius r_0. The strips in the contact region
122 form an angle θ^* with the cell axis satisfying $\cos \theta^* = r_0/r$. To weigh the relative importance of hydraulic
123 and frictional resistance, we introduced the non-dimensional quantity $\xi = \mu_{\text{wall}} \ell_c/(\alpha r)$, where μ_{wall} is the
124 wall-cell friction coefficient and α is a hydraulic resistance coefficient, Supplementary Note 4.

125   We first considered the limit of vanishing hydrodynamic resistance relative to wall friction, expressed
126 as $\xi \to +\infty$. In this situation, the cell velocity $v = -(1 - \cos \theta^*) c$ was obtained from the kinematics of the
127 propagating bulge by requiring no slippage between the pellicle and the wall, Fig. 3(c)i and Supplementary
128 Movie S9. This expression is consistent with the very small cell velocities at extreme confinement, where
129 $r \approx r_0$ or $\cos \theta^* \approx 1$, Fig. 2(c). To examine the effect of cell motion on the fluid inside the capillary in
130 this no-slip scenario, we evaluated with our model the induced water flow rate Q in either side of the bulge,
131 which we assumed to act as a hydraulic plug. Strikingly, we found that as cells crawl without sliding in a
132 given direction, they pump water in the opposite direction at a flow rate given by $Q = \pi r^2 (1 - \cos \theta^*) \cos \theta^* c$.
133 This counterintuitive hydraulic behavior results from the peristaltic shape changes of metaboly, and funda-
134 mentally differs from that of non-adherent polarized animal cells, which move like piston-like fixed-shape
135 *squirmers*.[24,28] We then reasoned that, if crawling *Euglena* cells in this limit were pumping fluid backwards,
136 then hydraulic resistance could in fact act as a propulsive force.

137   To test theoretically this idea, we placed ourselves in the opposite limit of vanishing wall friction relative
138 to hydraulic resistance, $\xi \to 0$, and computed cell velocity by requiring zero induced flow rate as the bulge
139 moves backwards. We found that in this scenario the pellicle slides relative to the wall. Furthermore,
140 instead of stalling under high hydraulic resistance like polarized animal cells,[24] peristaltic *Euglena* cells
141 actually move at a faster speed $v = -\left(1 - \cos^2 \theta^*\right) c$, Fig. 3(c)iii and Supplementary Movie S9. In an
142 intermediate regime, in which propulsion is governed by the balance of finite wall friction and hydrodynamic
143 resistance, our model predicted that cells are propelled by hydraulic resistance and dragged by wall friction,
144 opposite to polarized animal cells, Supplementary Note 4. In summary, despite seeming similarities between

4

the crawling modes of *Euglena* cells and of non-adherent polarized animal cells, our model highlighted fundamental differences associated with the large shape modulations of the former, and portrayed metaboly as a highly robust and adaptable mode of locomotion capable of using both frictional and hydraulic forces for propulsion depending on the mechanical nature of confinement. Furthermore, the fastest crawling cells in our experiments moved about 20 times faster than the fastest reported non-adherent polarized animal cells.[26]

One of the most striking predictions of this model is that confined *Euglena* cells, which act as hydraulic plugs, can move in a capillary without inducing any flow rate thanks to the shape deformations of metaboly. Supporting this prediction, we observed crawling cells accomplishing significant displacements next to stuck immobile cells, Fig. 3(d) and Supplementary Movie S10. In the absence of stuck cells, we visualized the flow generated by crawling cells tracking the motion of suspended micron-sized beads, Fig. 3(e) and Supplementary Movie S11. We found that beads in the vicinity of cells underwent rapid motions revealing local flows induced by shape changes and flagellar beating. These bead velocities, however, exhibited rapid decay away from the cell body, where they were consistent with Brownian motion in a quiescent fluid. Thus, in the light of our model, cells in our capillary experiments were close to the limit of high hydraulic resistance, which acted as the propulsive force. In agreement with this notion, we observed significant pellicle sliding in cells crawling and turning in a capillary, Fig. 3(f) and Supplementary Movies S5 and S12. By contrast and showing the robustness of metaboly, our model suggests that cells between glass plates, where hydraulic confinement is very low, crawled by exploiting frictional propulsion, Fig. 1(b) and Supplementary Movies S2 and S3.

Computational model

Our previous observations have established that *Euglena* cells develop highly concerted shape deformations to crawl under confinement, and that cells can adapt their gait to varying degrees of confinement between plates or in a capillary. We then tried to understand whether this complex adaptive behavior necessarily required a dedicated mechanosensing and mechanotransduction machinery or if, instead, the active pellicle could mechanically self-adapt its dynamics to a changing environment. To test this second possibility, we developed a theoretical and computational model of crawling in confinement by metaboly, which included the biological activity leading to strip sliding, the pellicle mechanics, and the interaction with the environment, Supplementary Note 5.

Despite similarities, the actuation mechanism and molecular players involved in metaboly are far less understood than those behind the much faster flagellar beating.[17] On the basis of calcium precipitation assays and reactivation of metaboly in detergent-extracted cell models, inter-strip sliding is thought to depend on molecular motors distinct from flagellar dyneins and associated to microtubules positioned along pellicular strips, which are locally and dynamically activated by the release/sequestration of cytoplasmic calcium from narrow subpellicular channels of endoplasmic reticulum.[6,29] In our model, we assumed that the space-time activation pattern driving cell deformations was unaffected by varying confinement, consistent with the confinement-independent period of metaboly, Fig. 2(d). We modeled the pellicle as an extended motor system, and its activation as a space-time modulation of the sliding velocity between adjacent strips in the absence of force, $v_{\text{motor}}^0(s, t)$ where s is arc-length along the strips and t is time, Fig. 4(a)i,ii. Forces between adjacent strips in the sliding direction can affect the velocity of the motor system. We considered an affine relation between the force experienced by the motor system, τ, and the actual sliding velocity, v_{motor}, Fig. 4(a)iii.[30,31] To determine the a priori unknown force distribution $\tau(s, t)$ acting on the extended motor system, we accounted for the pellicle elasticity and for its mechanical interaction with the environment, i.e. the cellular pressure to maintain cell volume constant, hydraulic forces required to push the water column, and contact/frictional forces against the capillary, Fig. 4(a)iv. We designed the activity pattern, Fig. 4(a)ii, to match the typical shape dynamics of metaboly at low confinement.[7] To solve the highly non-linear equations governing the active mechanics of the deformable pellicle under confinement, we developed a spline-based finite element computational method.

In the absence of confinement, this model rapidly reached a limit cycle (or gait) within a few periods, exhibiting the characteristic peristaltic cell deformations of metaboly, Supplementary Movie S13. As confinement incrementally constrained the shape excursions, we observed that the model self-adapted by developing a new limit cycle consistent with the imposed confinement, Fig. 4(b), which led to cell migration in the presence of frictional wall coupling and/or hydraulic resistance, see Fig. 4(c,d) for the limits of high hydraulic resistance and high friction. Remarkably, the computational model reproduced all the features of confined crawling by metaboly reported in Fig. 2, including the kinematics of the gait under confinement, Fig. 4(b,c), and the non-monotonic relation between capillary diameter and cell velocity, Fig. 4(d), which we attributed to a tradeoff between the ability to develop large shape excursions at low confinement and the sustained contact of the bulge running along a longer cell at high confinement. In agreement with the theoretical model in Fig. 3(c), the computational model also predicted faster motion in the limit of high fluid resistance, in which the maximum velocity agreed quantitatively with our experiments. Taken together, these results support a view of the pellicle of euglenids as an elastic and extended motor system that, once biologically activated, can mechanically self-adjust to the degree of confinement to produce an effective gait.

Outlook

We have thus established that, in analogy with the mesenchymal-to-amoeboid transition of animal cells[26] or the amoeboid-to-flagellar transition of *Naegleria gruberi*,[32] *Euglena gracilis* develop a transition between flagellar and metaboly modes of locomotion triggered by confinement. Biophysically, the peristaltic movement of *Euglena* during metaboly provides a new and remarkably robust mechanism of fast cell crawling. It is unclear, however, whether *Euglena* take advantage of this capability in natural conditions, where they predominantly swim in the water column. How and why *Euglena* cells retained an active pellicle, a vestige of a phagotrophic ancestry, and developed the ability to operate this machine in a non-reciprocal manner compatible with effective crawling is intriguing, as further emphasized by our examination of confined metaboly in a primary osmotrophic and a phagotrophic species of euglenids (Supplementary Note 6). From an engineering point of view, the ability of the pellicle to mechanically self-adapt and maintain the locomotory function under different geometric and mechanical conditions represents a remarkable instance of mechanical or embodied intelligence,[33,34] a design principle in bio-inspired robotics by which part of the burden involved in controlling complex behaviors is outsourced to the mechanical compliance of the materials and mechanisms that build the device.

Author Contributions

GN, MA and ADS conceived the study; AB provided cells and culture expertise; GN performed the experiments; GN, MA and ADS analyzed the data, performed theoretical analysis and wrote the paper.

References

[1] Buetow, D. E. *The Biology of Euglena: Physiology*. The Biology of Euglena. Academic Press, New York (1982).

[2] Leander, B. S. Euglenida. euglenids or euglenoids. Version 10 November 2012. http://tolweb.org/Euglenida/97461/2012.11.10 in The Tree of Life Web Project, http://tolweb.org/ (2012).

[3] Leander, B. S., Lax, G., Karnkowska, A. & Simpson, A. G. B. Euglenida. In: Archibald, J. et al. (eds) *Handbook of the Protists*. Springer, Cham (2017).

[4] Dobell, C. *Antony van Leeuwenhoek and his "Little Animals"*. Dover, New York (1932).

[5] Suzaki, T. & Williamson, R. E. Euglenoid movement in *Euglena fusca*: Evidence for sliding between pellicular strips. *Protoplasma* **124,** 137-146 (1985).

[6] Suzaki, T. & Williamson, R. E. Reactivation of the euglenoid movement and flagellar beating in detergent-extracted cells of *Astasia longa*: Different mechanisms of force generation are involved. *J. Cell Sci.* **80,** 75-89 (1986).

[7] Arroyo, M., Heltai, L., Millán, D. & DeSimone, A. Reverse engineering the euglenoid movement. *Proc. Natl. Acad. Sci. USA* **109,** 17874-9 (2012).

[8] Fletcher, D. A. & Theriot, J. A. An introduction to cell motility for the physical scientist. *Phys. Biol.* **1,** T1-T10 (2004).

[9] Avron, J. E., Kenneth, O. & Oaknin, D. H. Pushmepullyou: An efficient micro-swimmer. *New J. Phys.* **7,** 234 (2005).

[10] Rossi, M., Cicconofri, G., Beran, A., Noselli, G. & DeSimone, A. Kinematics of flagellar swimming in *Euglena gracilis*: Helical trajectories and flagellar shapes. *Proc. Natl. Acad. Sci. USA* **114,** 13085-13090 (2017).

[11] Yamaguchi, A., Yubuki, N. & Leander, B. S. Morphostasis in a novel eukaryote illuminates the evolutionary transition from phagotrophy to phototrophy: description of *Rapaza viridis* n. gen. et sp. (Euglenozoa, Euglenida). *BMC Evol. Biol.* **12,** 29 (2012).

[12] Leander, B. S., Esson, H. J. & Breglia, S. A. Macroevolution of complex cytoskeletal systems in euglenids. *BioEssays* **29,** 987-1000 (2007).

[13] Karnkowska, A. et al. Phylogenetic relationships and morphological character evolution of photosynthetic euglenids (Excavata) inferred from taxon-rich analyses of five genes. *J. Eukaryot. Microbiol.* **62,** 362-373 (2015).

[14] Esson, H. J. & Leander, B. S. Novel pellicle surface patterns on *Euglena obtusa* (euglenophyta) from the marine benthic environment: Implications for pellicle development and evolution. *J. Phycol.* **44,** 132-141 (2008).

[15] Jennings, H. S. *Contributions to the study of the behaviour of lower organisms*. Carnegie Institution of Washington (1904).

[16] Suzaki, T. & Williamson, R. E. Cell surface displacement during euglenoid movement and its computer simulation. *Cell Motil. Cytoskel.* **6,** 186-192 (1986).

[17] Lin, J. & Nicastro, D. Asymmetric distribution and spatial switching of dynein activity generates ciliary motility. *Science* **360,** 396 (2018).

[18] Arroyo, M. & DeSimone, A. Shape control of active surfaces inspired by the movement of euglenids. *J. Mech. Phys. Solids* **62,** 99-112 (2014).

[19] Milo, R. & Phillips, R. *Cell Biology by the Numbers*. Garland Science, New York (2015).

[20] Purcell, E. M. Life at low Reynolds numbers. *Am. J. Phys.* **45,** 3-11 (1977).

[21] Wu, H. et al. Amoeboid swimming in a channel. *Soft Matter* **12,** 7470-7484 (2016).

[22] Hawkins, R. J. et al. Pushing off the walls: A mechanism of cell motility in confinement. *Phys. Rev. Lett.* **102,** 1-4 (2009).

[23] Hawkins, R. J. et al. Spontaneous contractility-mediated cortical flow generates cell migration in three-dimensional environments. *Biophys. J.* **101,** 1041-1045 (2011).

[24] Bergert, M. et al. Force transmission during adhesion-independent migration. *Nat. Cell Biol.* **17,** 524-529 (2015).

[25] Prentice-Mott, H. V. et al. Biased migration of confined neutrophil-like cells in asymmetric hydraulic environments. *Proc. Natl. Acad. Sci. USA* **110,** 21006-21011 (2013).

[26] Liu, Y. J. et al. Confinement and low adhesion induce fast amoeboid migration of slow mesenchymal cells. *Cell* **160,** 659-672 (2015).

[27] Moreau, H. D. et al. Macropinocytosis overcomes directional bias due to hydraulic resistance to enhance space exploration by dendritic cells. BioRxiv preprint available at https://doi.org/10.1101/272682 (2018).

[28] Lighthill, M. J. On the squirming motion of nearly spherical deformable bodies through liquids at very small Reynolds numbers. *Commun. Pur. Appl. Math.* **5,** 109-118 (1952).

[29] Murray, J. M. Control of cell shape by calcium in the *Euglenophyceae*. *J. Cell Sci.* **49,** 99-117 (1981).

[30] Svoboda, K. & Block, S. M. Force and velocity measured for single kinesin molecules. *Cell* **77,** 773-784 (1994).

[31] Abraham, Z., Hawley, E., Hayosh, D., Webster-Wood, V. A. & Akkus, O. Kinesin and dynein mechanics: Measurement methods and research applications. *J. Biomech. Eng.* **140,** 020805-020805-11 (2018).

[32] Fritz-Laylin, L. K. et al. The genome of *Naegleria gruberi* illuminates early eukaryotic versatility. *Cell* **140,** 631-642 (2010).

[33] Pfeifer, R., Lungarella, M. & Iida, F. Self-organization, embodiment, and biologically inspired robotics. *Science* **318,** 1088-1093 (2007).

[34] Kim, S., Laschi, C. & Trimmer, B. Soft robotics, a bio-inspired evolution in robotics. *Trends Biotechnol.* **31,** 287-294 (2013).

Figure captions

Figure 1: Confinement triggers changes in cell behavior and metaboly. (a) *Euglena* cells in dilute cultures (i) exhibited fast flagellar swimming without cell shape changes, at typical speeds of $68.2 \pm 1.13\,\mu$m/sec (SEM, n=50) or 1.31 ± 0.03 body lengths/sec (SEM, n=50). In crowded cultures (ii) cells displayed a variety of behaviors, including fast flagellar swimming (yellow arrow), cell rounding and spinning (red arrow), and large amplitude cyclic cell body deformations – metaboly (purple ellipse), Supplementary Movie S1. (b) When confined between glass plates, cells systematically developed metaboly. Observation using brightfield reflected light microscopy revealed the reconfigurations of the striated cell envelope (pellicle) concomitant with cell deformations in the plane of the glass plate (n=5 cells), Supplementary Movies S2 and S3. (c) Schematic representation of the pellicle, the strip separation w, and the local mechanism of active deformation of the pellicle, according to which the relative sliding between strips produces a shear strain γ along the direction of the strips. During the shape dynamics in (b) w remained nearly constant (559 ± 0.003 nm, SEM, n=100). (d) According to a mathematical model for the kinematics of the pellicle (Supplementary Note 1), the rate of change of γ with arc-length s along a strip (measured from the anterior end) is given by the curvature of the strip κ. By selecting strips in (b) emanating from the pole, where sliding is geometrically constrained, we could quantify the sliding displacement between adjacent strips $w\gamma$ required to bend an initially straight strip (e), where the color-coding matches the strips highlighted in (b). (f) Cells swimming into tapered capillaries transitioned from fast flagellar swimming (i) to developing large amplitude shape excursions (ii) including rounding (iii) and the prototypical highly orchestrated peristaltic cell deformations of metaboly (iv), Supplementary Movie S4. This transition between (i) and (ii) occurred at a ratio between capillary and cell diameter of about 2.1 ± 0.05 (SEM, n=10).

Figure 2: Metaboly is an effective crawling mode of locomotion under confinement. (a) At low confinement, the bulge traveling backwards along the cell body transiently contacted the capillary walls, producing a net forward motion (i). At higher confinement, cells adapted the gait, with a larger contact area of the bulge and smaller amplitude of cell deformations. However, the crawling mechanism remained the same (ii). (b) Kymographs of crawling *Euglena gracilis* under increasing confinement show the regularity of the gait, the backward bulge motion, and the forward cell motion. Crawling by metaboly was effective up to very large degrees of confinement (see the insets and Supplementary Movie S6). The normalized velocity expressed in cell body lengths per period was maximum at an intermediated capillary diameter (c), whereas the period of the gait was largely insensitive to confinement (d). The blue dashed lines in (c) and (d) are guides to the eye. The capillary diameter d_{cap} was normalized by the cell diameter d_{cell} as it was free-swimming with a fixed cigar shape in the wider part of the capillary ($d_{cell} \simeq 9\,\mu m$). The error bars in (c) and (d) refer to the standard error of the mean and the size of samples is indicated. Here one sample is a complete period, and data was gathered from 16 cells.

Figure 3: Mechanism of locomotion during metaboly. (a) (i) Canonical model of propulsion of non-adherent polarized animal cells under confinement: frictional forces induced by actin retrograde flow propel the cell forward against resistive hydraulic forces required to displace the water column in the capillary. (ii) In *Euglena* cells crawling by metaboly, the backward-moving pellicle bulge is analogous to actin retrograde flow in animal polarized cells. (b) Kinematics of the theoretical model for the power phase of metaboly. (i) Transformation of an idealized cylindrical pellicle by a uniform shear γ along the strips. (ii) By propagating a pellicle shear profile $\bar{\gamma}(s)$ along the cell body following $\gamma(s,t) = \bar{\gamma}(s - ct)$, we model a moving localized bulge, which with our sign convention, moves leftwards at speed $c < 0$ in the frame of the cell. (c) In the limit of infinite frictional coupling relative to hydraulic resistance (i), cell velocity is determined by the no-slip condition in the contact region. As indicated by the blue control volume, metaboly then results in net water pumping in the direction opposite to cell motion. The average fluid velocity v_f is defined as the flow rate Q divided by the cross-sectional area of the capillary. In the limit of zero frictional coupling relative to hydraulic resistance (iii), cell velocity is determined by the no water pumping condition, cells are fastest, and the pellicle slides in the contact region, as indicated by the red arrows. In intermediate cases (ii), hydraulic forces (propulsive) and frictional forces (resistive) compete, there is some degree of sliding and pumping, and the cell velocity is intermediate. (d) Kymograph of an immobile cell next to another cell crawling by metaboly, Supplementary Movie 10. (e) Quantification of fluid flow around crawling cells tracking suspended beads. Error bars refer to the standard error of the mean and sample size is indicated (a sampling point is the instantaneous velocity of a bead between two frames, data from 2 cells and 21 bead trajectories). (f) Kymograph made from images intermittently focused at the capillary wall to visualize the pellicle and at the capillary axis to visualize cell shape. The trajectories of pellicle features (yellow curve) reveal sliding between the pellicle and the capillary wall in the contact region.

Figure 4: Computational modeling of crawling in confinement by metaboly. (a) Model ingredients. (i) The pellicle is viewed as an elastic and extended motor system, modeled by an axisymmetric continuum surface with a field of material orientations converging towards two poles and accounting for the configuration of strips. The activation of this motor system in space (along the arc-length of strips, s) and time, t, is modulated to drive shape changes. Activation is modeled by the sliding velocity between adjacent strips in the absence of force, $v_{\mathrm{motor}}^0(s,t)$. (ii) Time-periodic pattern of the activation $v_{\mathrm{motor}}^0(s,t)$ during two gaits, in units of strip separation w per period T. (iii) The actual sliding velocity v_{motor} is modified by distributed forces along adjacent strips in the sliding direction, τ. We model the force-dependent velocity of the motor system with an affine relation characterized by the time and space dependent v_{motor}^0 and by a stall force τ_{stall} of fixed magnitude, see Supplementary Note 5 for a discussion. (iv) The distributed force acting on the motor system, $\tau(s,t)$, is determined by the mechanical interactions of the pellicle with its environment (cellular pressure; contact, frictional and hydraulic forces) and by the pellicle mechanics, which include bending elasticity and stretching elastic forces that penalize deviations between the actual pellicle shear-rate and that imposed by the motion of motors, $v_{\mathrm{motor}}(s,t)/w$. (b) Selected snapshots during the gait at four degrees of confinement. (c) Kymographs obtained from simulations in the high fluid resistance (i) and the high wall friction (ii) limits at the same four degrees of confinement. The contact region is colored in orange and the lines represent trajectories of material particles on the pellicle surface, showing sliding in the hydraulic-dominated case and no sliding in the friction-dominated case. Induced flow rate, normalized by the maximum cell velocity times the capillary cross-sectional area, is represented by gray curves in the case of high friction; it is zero in the limit of high hydraulic resistance. (d) Normalized cell velocity in body lengths per period as a function of normalized capillary diameter predicted by the simulations.

Methods

Culture of cells

Strain SAG 1224-5/27 of *Euglena gracilis* obtained from the SAG Culture Collection of Algae at the University of Göttingen (Germany) was maintained axenic in liquid culture medium Eg. Cultures were transferred weekly. Heterotrophic *Distigma proteus* and *Peranema trichophorum* were obtained from Sciento (https://www.sciento.co.uk). Subcultures of *P. trichophorum* were established in Eau Volvic with *Chlorogonium capillatum* (SAG 12-2b) as food source. All cells were kept in sterile 16 mL polystyrene test tubes in an incubator IPP 110 plus from Memmert at 15 °C and at a light:dark cycle of 12:12 h under cold white LED illumination with an irradiance of about 50 µmol/(m^{2}s).

Imaging of cells and preparation of tapered capillaries

An Olympus BX 61 upright microscope with motorized stage was employed in all experiments. These were performed at the Sensing and Moving Bioinspired Artifacts Laboratory of SISSA. Typically, the microscope was equipped with a LCAch 40X Ph2 objective (NA 0.55) for the imaging of cells behavior in capillaries using transmitted brightfield illumination. A Plan N 10X objective (NA=0.25) was employed to image cells and 1 µm in diameter polystyrene beads by combining brightfield and fluorescence microscopy (Supplementary Note 1 and Supplementary Movies S7 and S11). The visualization of pellicle strips between microscope slides and in glass capillaries was achieved by exploiting brightfield reflected light microscopy and using a UPlanFL N 100X objective (NA 1.30 Oil). Micrographs were recorded with a CMOS digital camera from Basler (model acA2000-50gm) at a frame rate of either 20 fps or 40 fps. The higher acquisition rate of 40 fps was employed to time-resolve the dynamics of pellicle strips reconfigurations and for the study of wall friction as reported in Supplementary Note 2. Tracking of fluorescence beads was performed using Particle Tracker 2D/3D of the MosaicSuite for ImageJ.[35] Tapered capillaries of circular cross section were obtained from borosilicate glass tubes (Sutter Instrument, model B100-30-7.5HP) by employing a micropipette puller (Sutter Instrument, model P-97). A typical profile of such a capillary measured from micrographs is represented in Supplementary Fig. 2(b). At each trial a glass capillary was filled with a diluted solution of cells in culture medium Eg and fixed to the microscope stage by means of a custom made, 3d-printed holder. To avoid optical aberrations that could arise from the curvature of the external surface of the capillary, this was positioned between two 0.17 mm coverslips and covered with microscopy immersion oil.

Estimation of cell area and volume

To estimate the area and volume of cells sandwiched between microscope glass slides, we measured the surface area S and perimeter P of the part of the cell surface in contact with the glass slides by focusing the microscope on these planes. We approximated the surface area of the cell envelope as $S_{\text{cell}} = 2S + \pi HP/2$ and its volume by $V_{\text{cell}} = SH + \pi H^2 P/8$, which assumes that cross-sections of the part of the cell surface not in contact with the plates are half circles. Using 15 frames from Supplementary Movie S3, where $H = 4.3$ µm, we estimated using this method $S_{\text{cell}} \approx 1887$ µm^2 ± 2% and $V_{\text{cell}} \approx 3283$ µm^3 ± 1%.
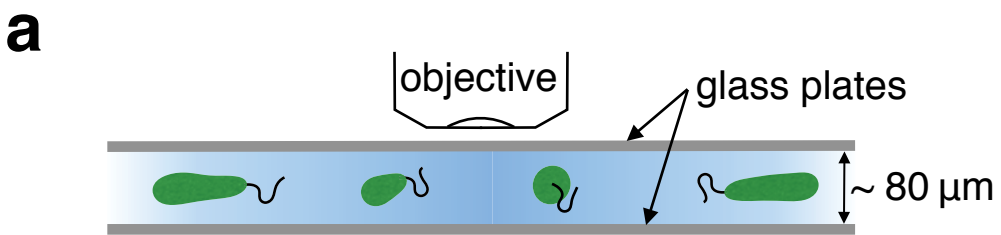
Code availability

Mathematica (version 11.3.0.0) custom algorithms were developed and used to analyze the theoretical model in Fig. 3 and Supplementary Note 4. Matlab (R2017b) custom algorithms were developed and used to compute sliding displacements from strip curvature (Fig. 1(e) and Supplementary Note 1) and to implement the computational model in Fig. 4 and Supplementary Note 5. These computer codes are available from the corresponding authors upon reasonable request.
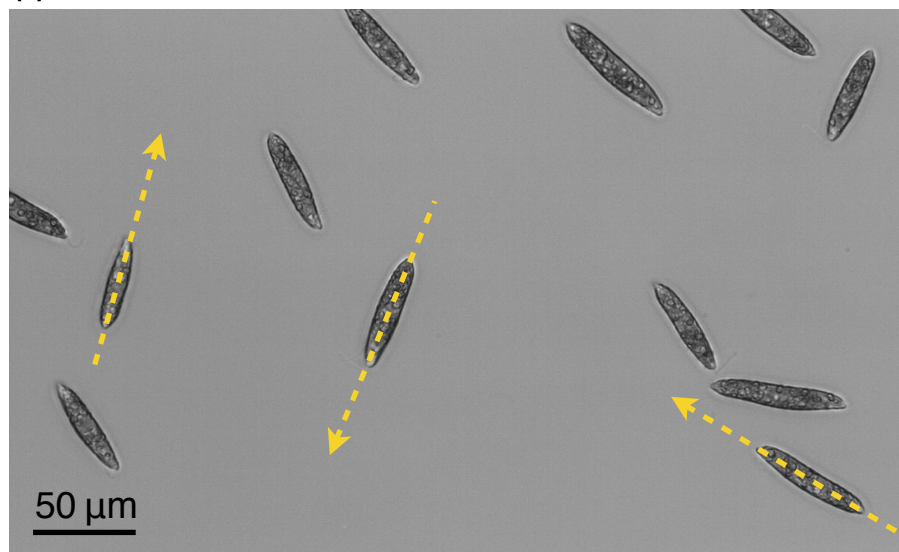
Data availability

The data that support the plots within this paper and other findings of this study are available from the corresponding authors upon request.
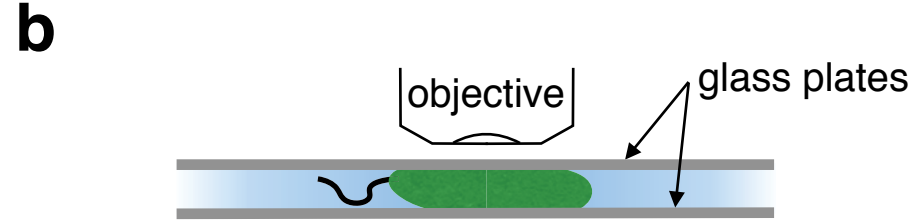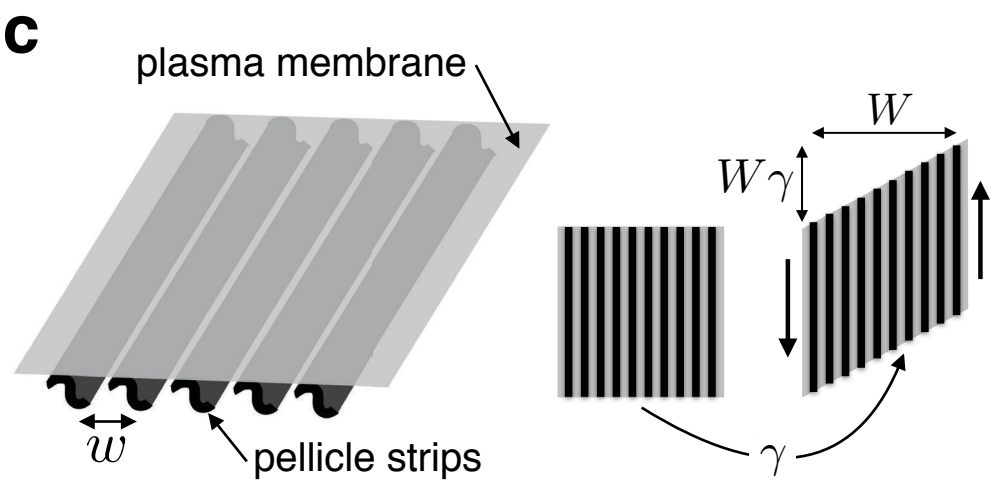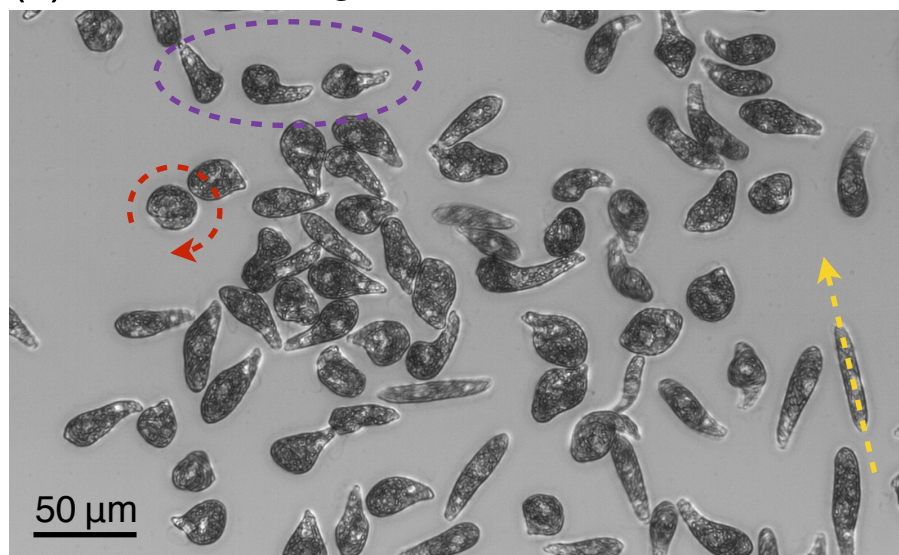
References

[35] Sbalzarini, I. & Koumoutsakos, P. Feature point tracking and trajectory analysis for video imaging in cell biology. *J. Struct. Biol.* **151,** 182-195 (2005).
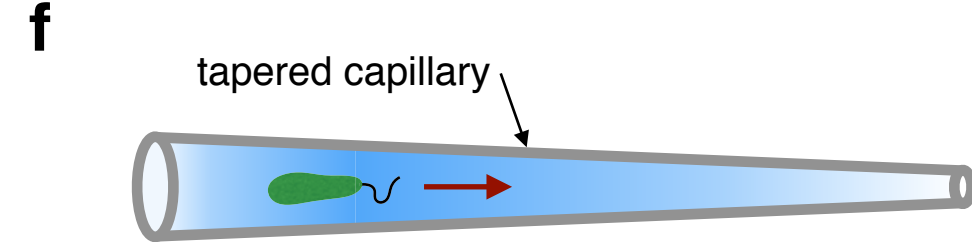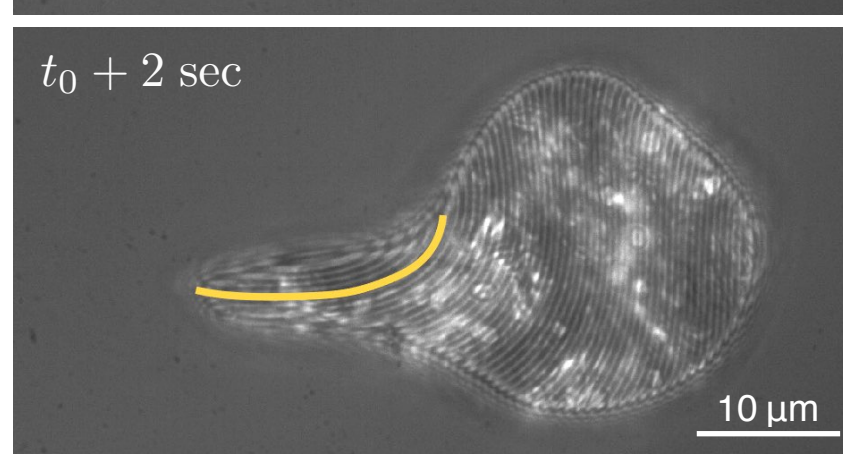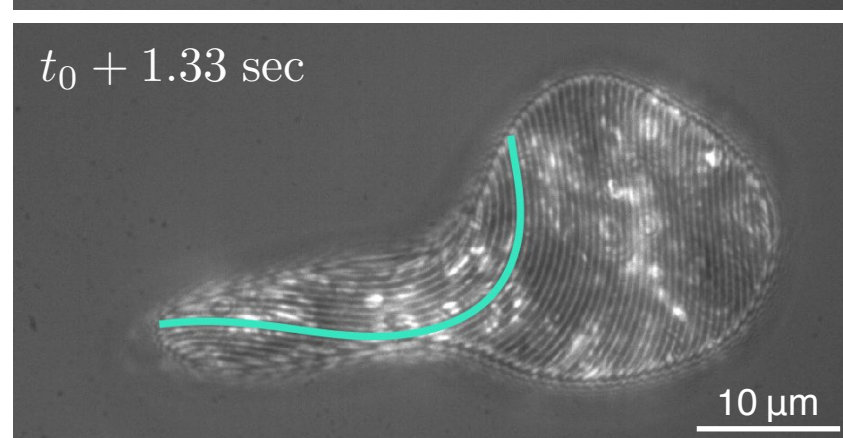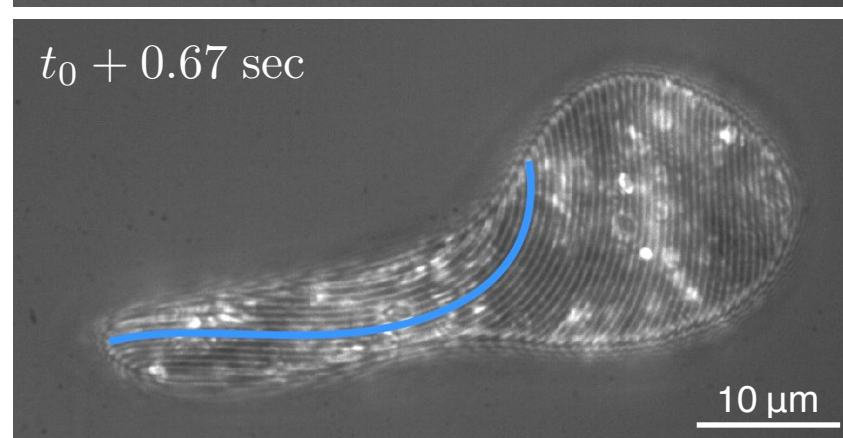
a

objective   glass plates

~ 80 μm

(i) Dilute *Euglena* culture

50 μm

(ii) Crowded *Euglena* culture

50 μm

c

plasma membrane

W

$W\gamma$

w pellicle strips γ

b

objective   glass plates

Pellicle reconfiguration during metaboly

t_0

10 μm

$t_0 + 0.67$ sec

10 μm

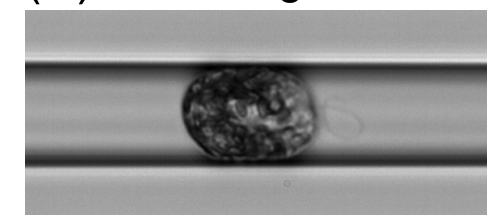$t_0 + 1.33$ sec

10 μm

$t_0 + 2$ sec

10 μm
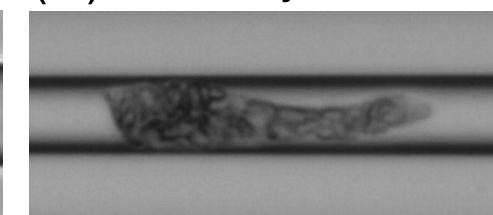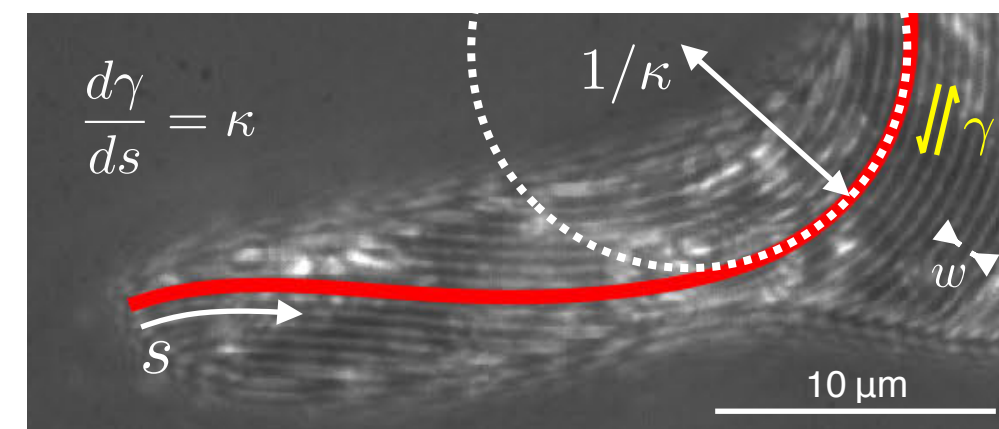
f

tapered capillary
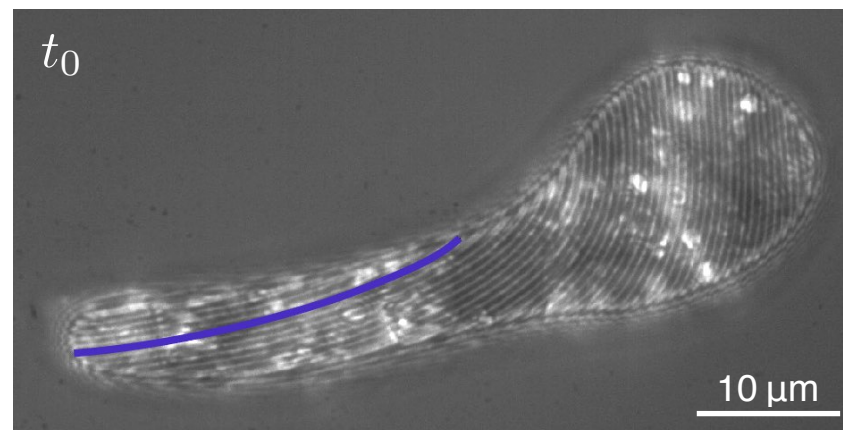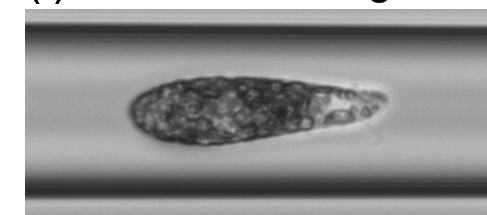
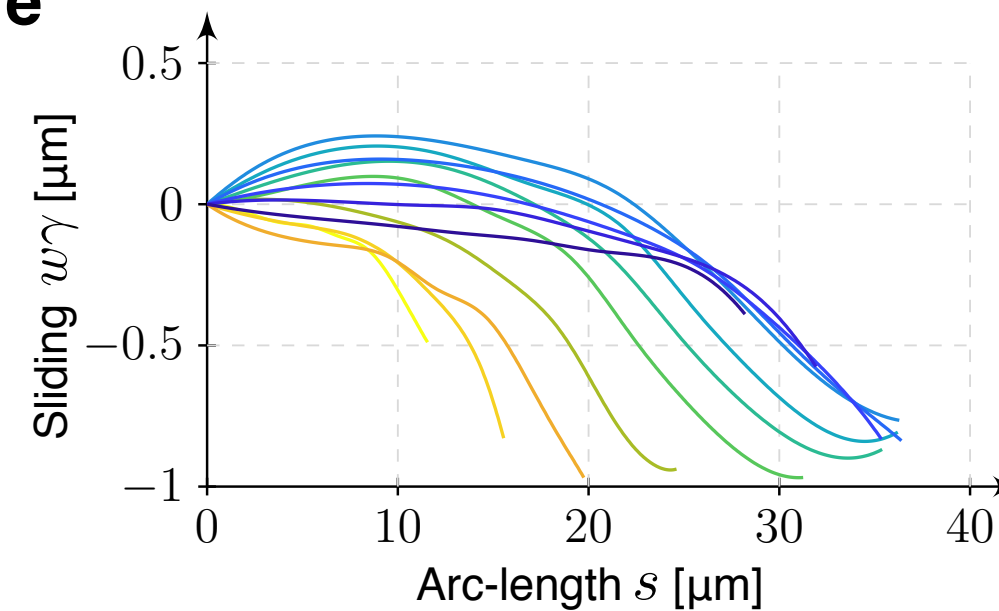**(i) Free swimming**   **(ii) Cell deformation**
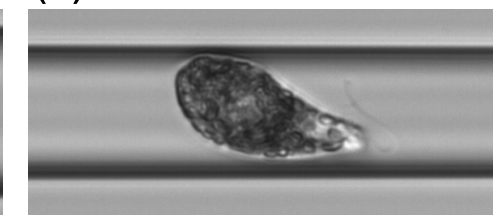
(iii) Rounding   **(iv) Metaboly**

d

$\dfrac{d\gamma}{ds} = \kappa$

$1/\kappa$

γ

w

s

10 μm

e

Sliding $w\gamma$ [μm]

Arc-length s [μm]

a

(i) Bulge at low confinement
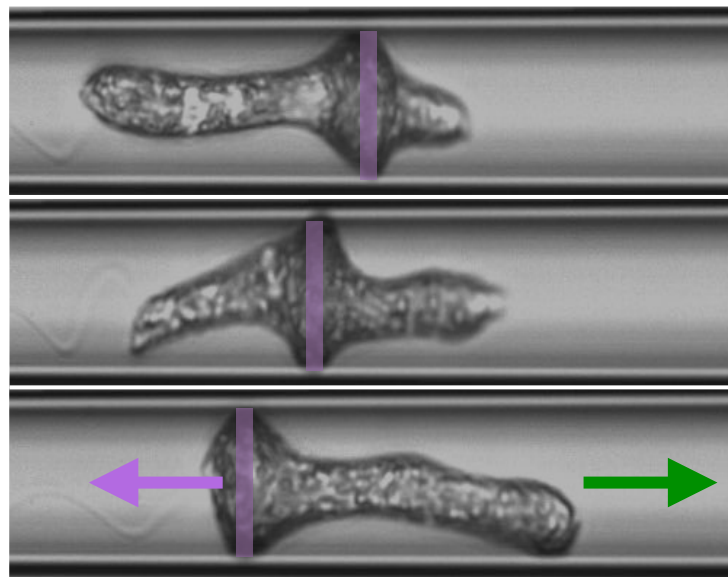
backward motion of the bulge in contact

forward motion of the cell

(ii) Bulge at higher confinement

b

space

time

10 s

20 μm

d_{cap}

$d_{cap}/d_{cell} = 1.95$

backward bulge motion

$d_{cap}/d_{cell} = 1.3$

forward cell motion

$d_{cap}/d_{cell} = 1.0$

$d_{cap}/d_{cell} = 0.85$

c

Normalized cell velocity

Normalized capillary diameter

17
55
54
6
7
10
12

d

Cell gait period [s]

Normalized capillary diameter

17
55
54
6
7
10
12
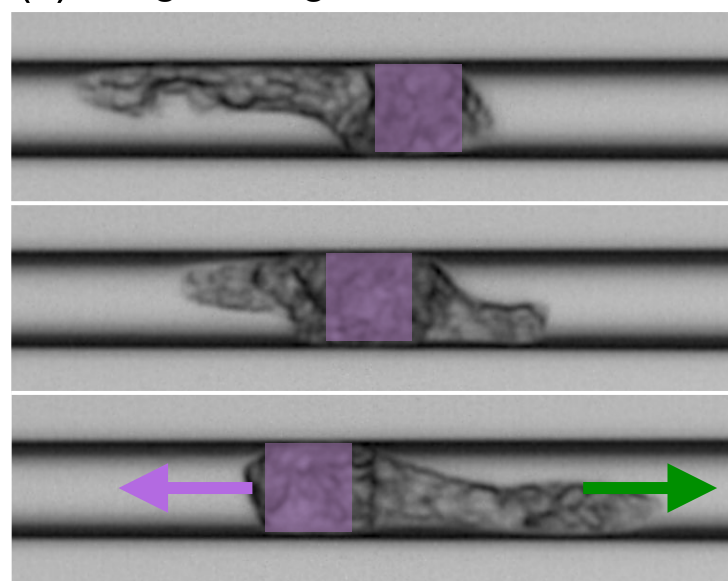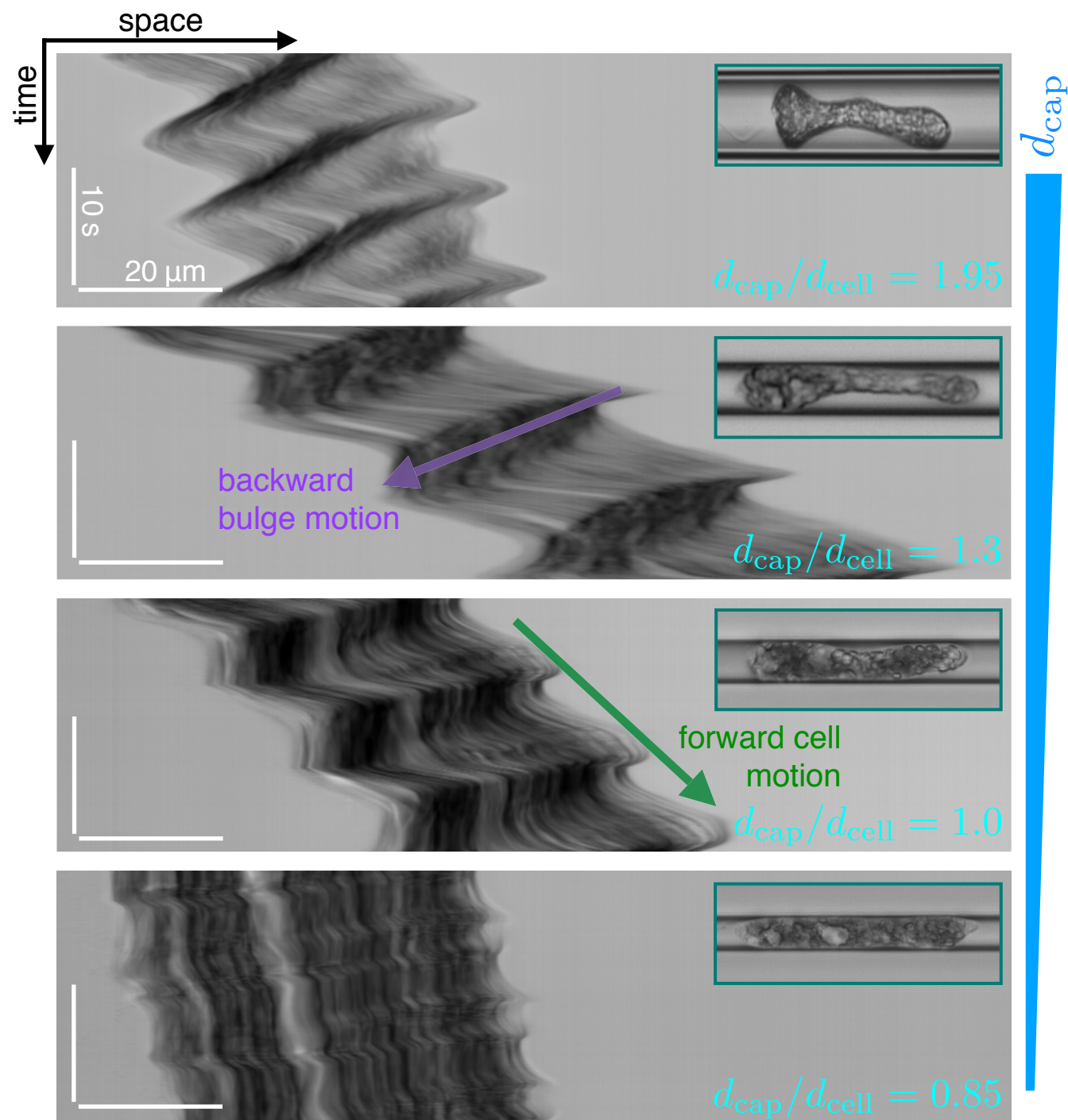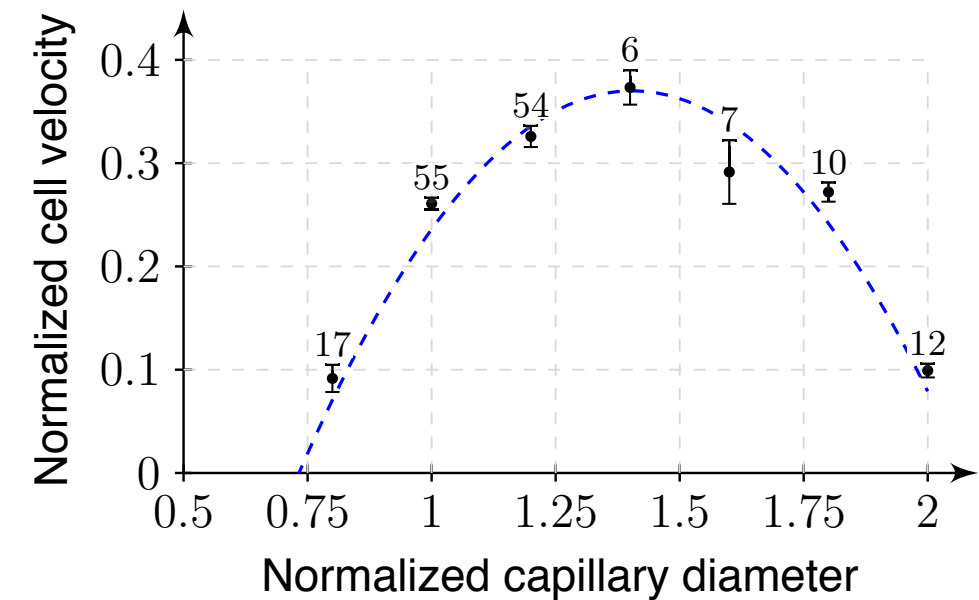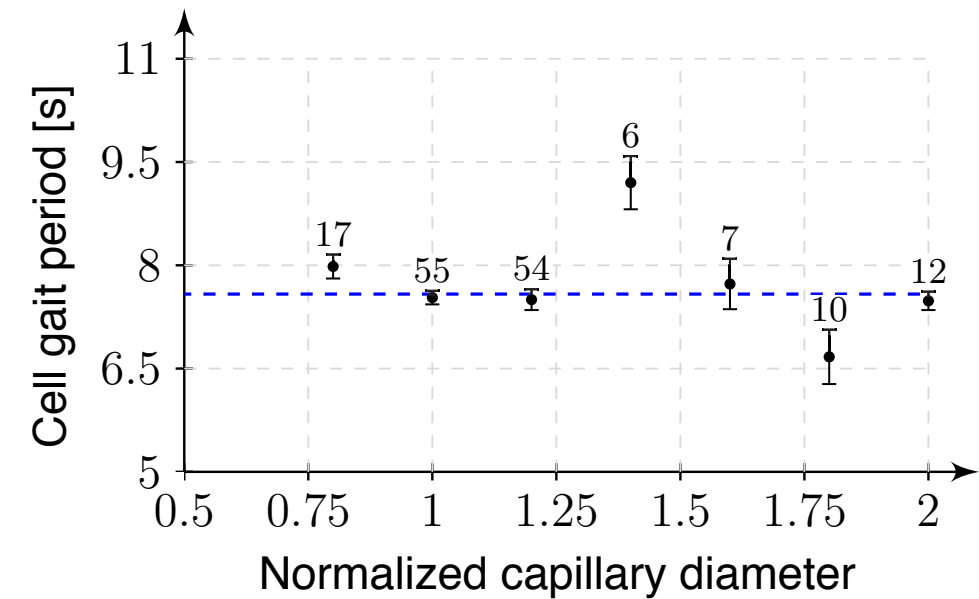
a

(i) Confined locomotion of non-adherent polarized animal cell

retrograde flow

cell motion

resistive hydrodynamic force

propulsive frictional force
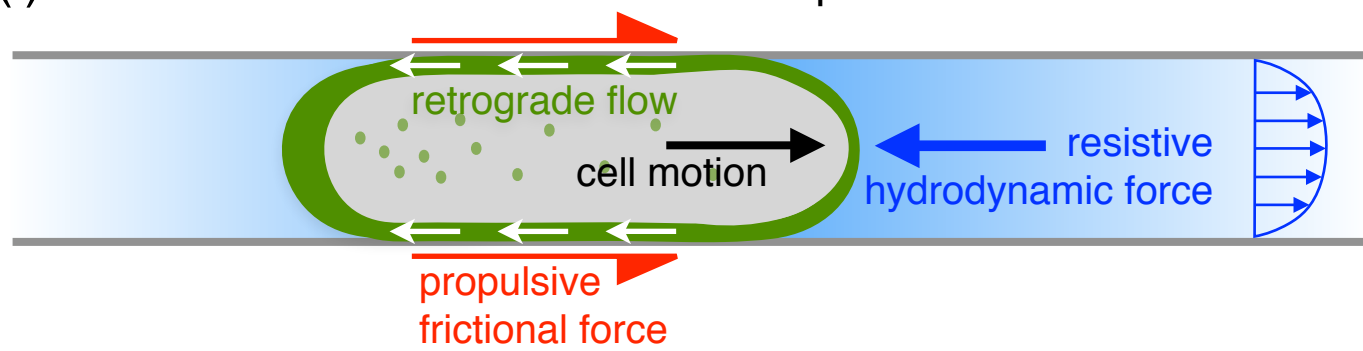
(ii) Confined locomotion of *Euglena* performing metaboly

cell motion

backward bulge motion

b

(i) s — uniform γ

(ii) s — $\gamma(s,t)$

γ — s

backward shearing wave

c

θ^*

r — r_0

ℓ_c

c

— Reference configuration

$t=0$

material particle — cell tip — fluid

(i) High friction

$t=\delta t$

$v_f \delta t$
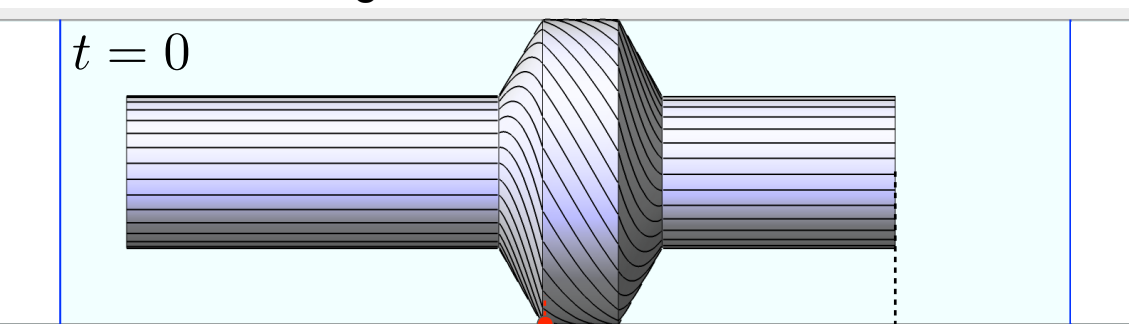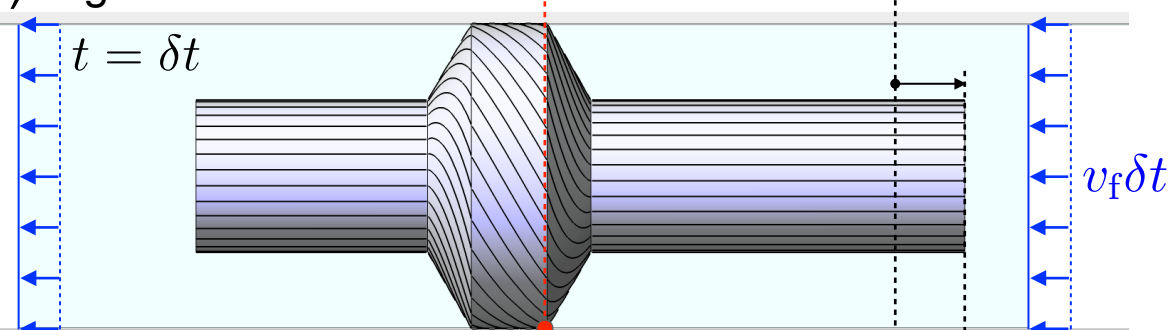
(ii) Intermediate case

$t=\delta t$

(iii) High hydraulic drag

$t=\delta t$

$v\delta t$

$v_s \delta t$

d

immobile cell — crawling cell

space

time

20 s

50 μm

e

crawling cell — fluorescent bead

50 μm

415 318
555 432
664 710
825 706
381 379
176
91 136
144 193
499
627 785
892 568
560 631
412 529
667 654

Beads velocity [μm/s]

Distance from cell center [μm]

f

space

time

motion of cell edges (focus at the capillary axis)

sliding of pellicle strips (focus at the capillary wall)

10 s

10 μm
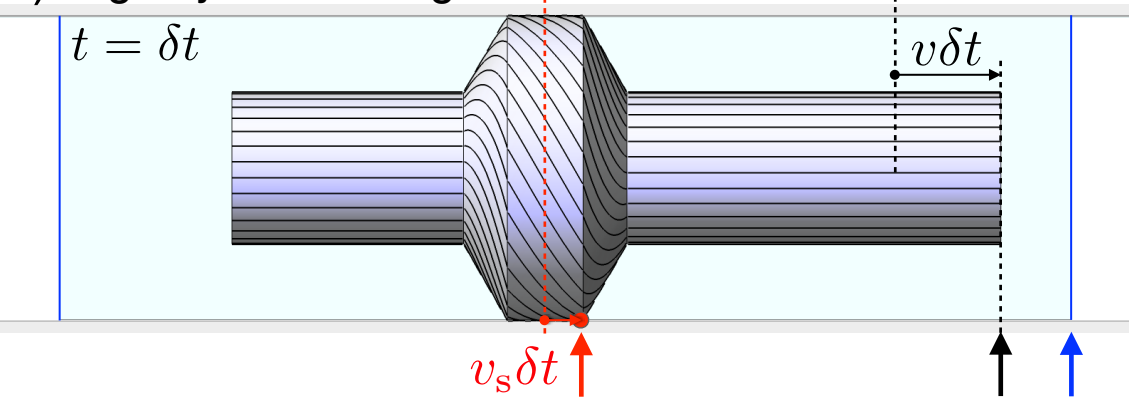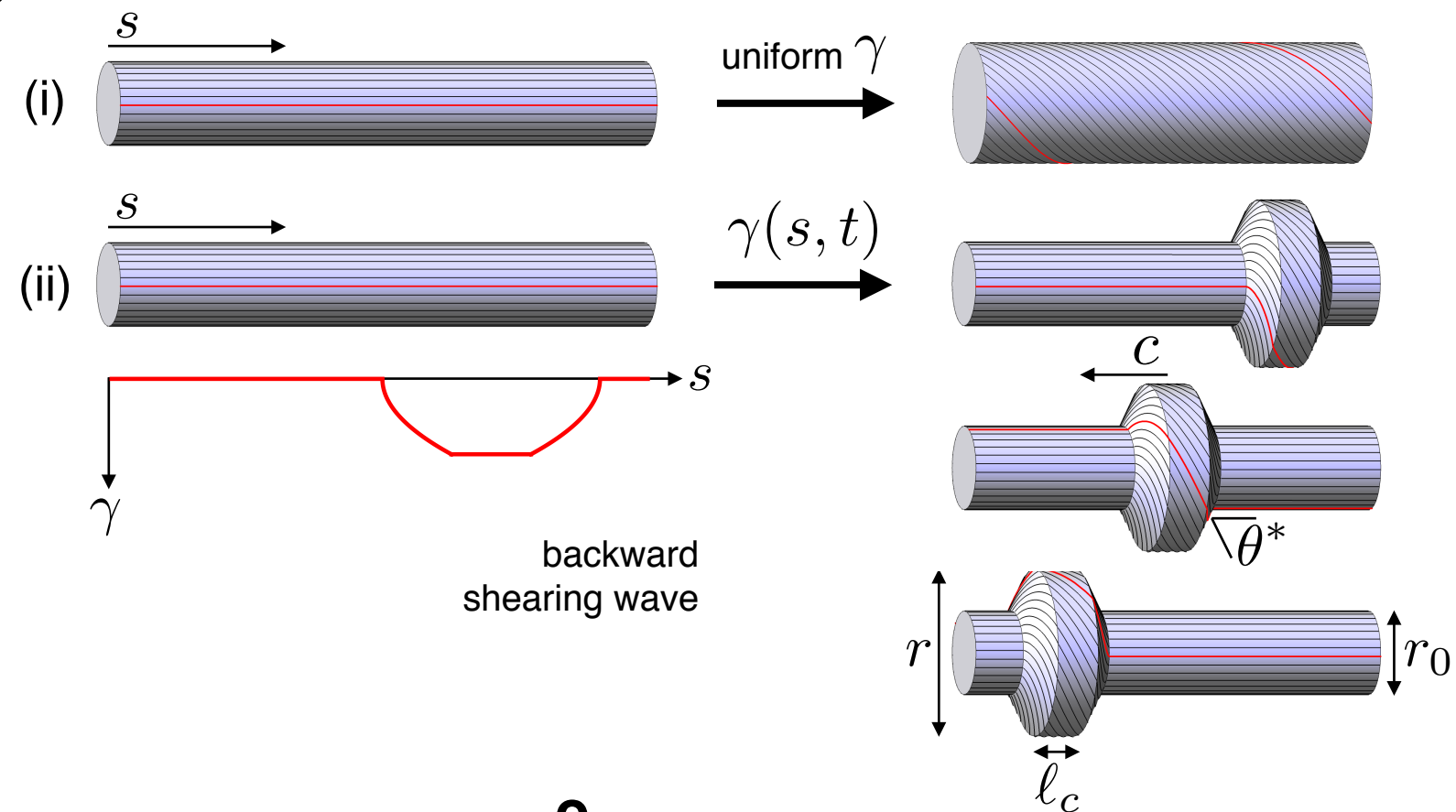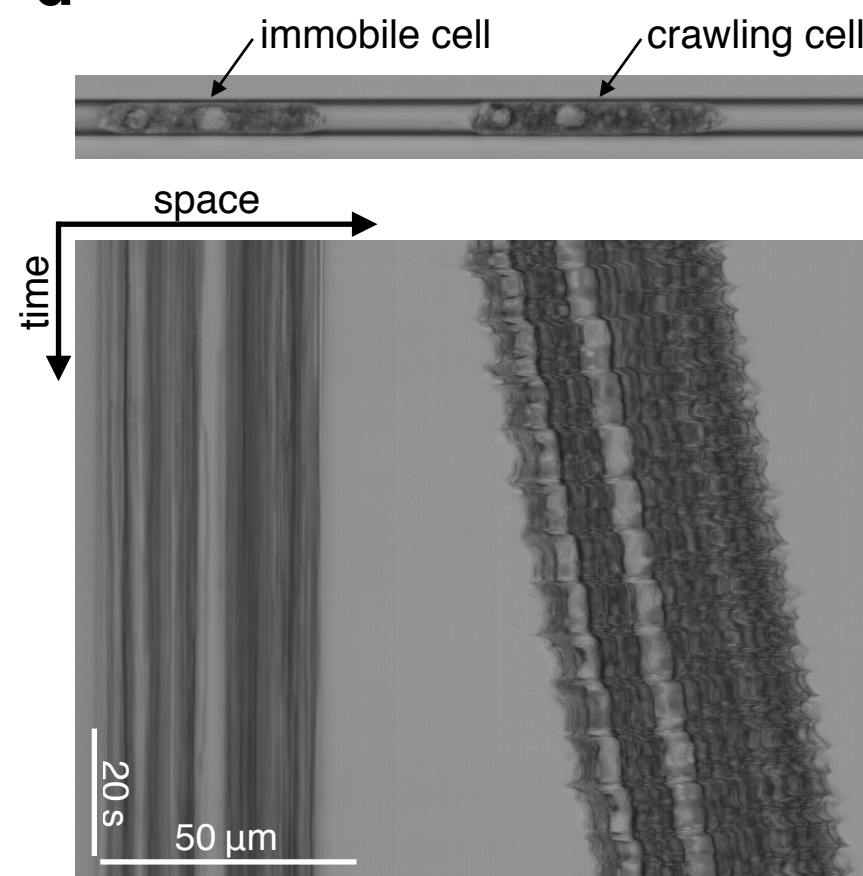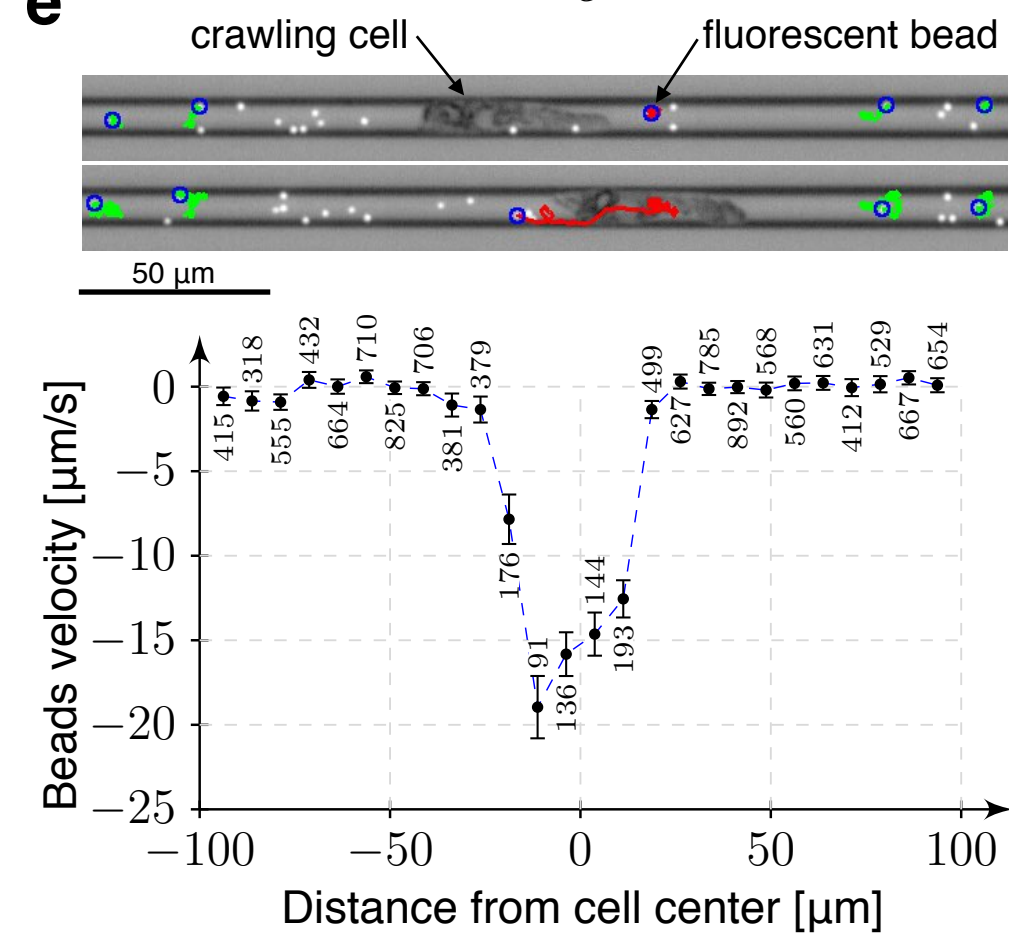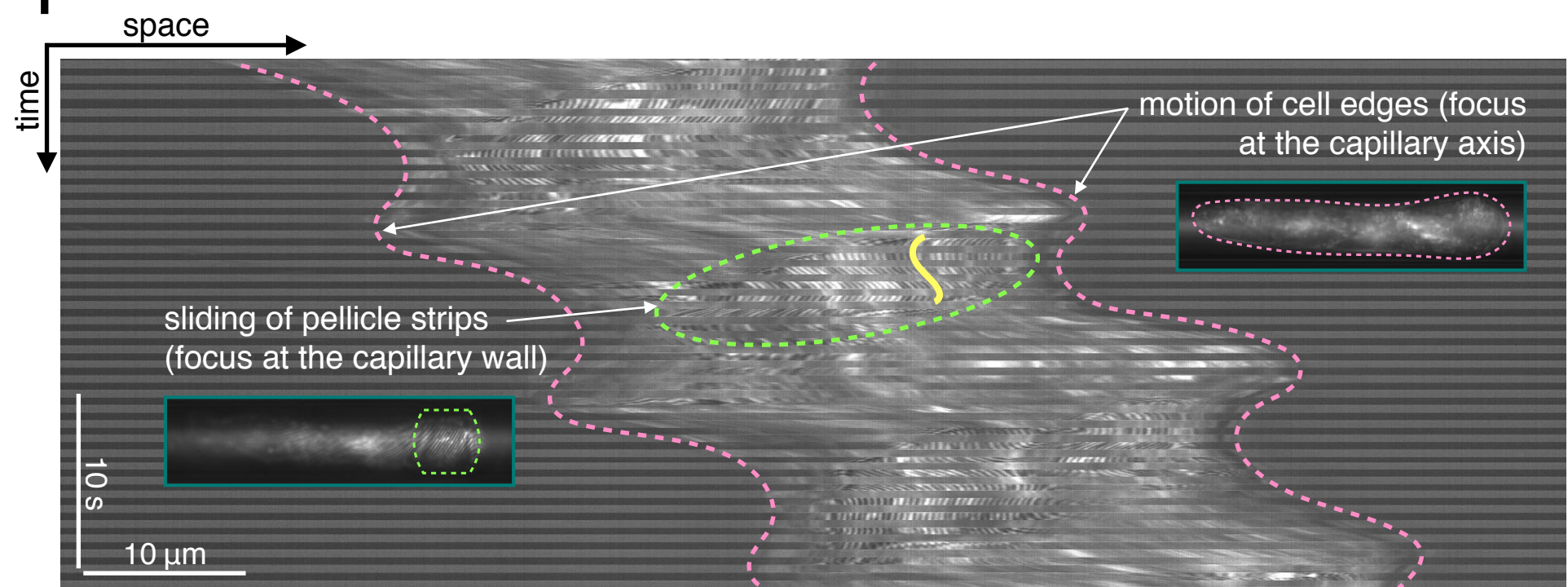
a

(i) Extended and elastic motor system
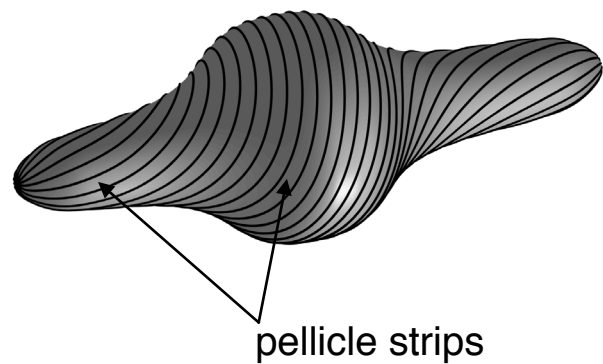
pellicle strips

(ii) Time-periodic activation pattern: $v_{\mathrm{motor}}^0(s,t)\,T/w$
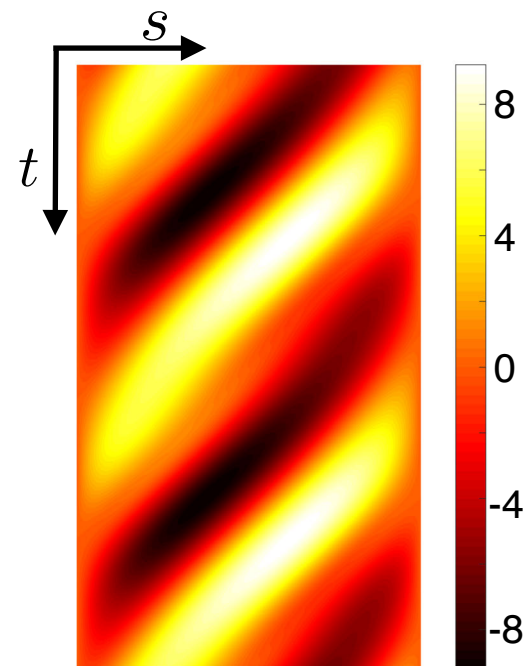
(iii) Dependence of motor system velocity on forces along strips

v_{motor}

v_{motor}^0

τ_{stall}

$-\tau_{\mathrm{stall}}$

τ
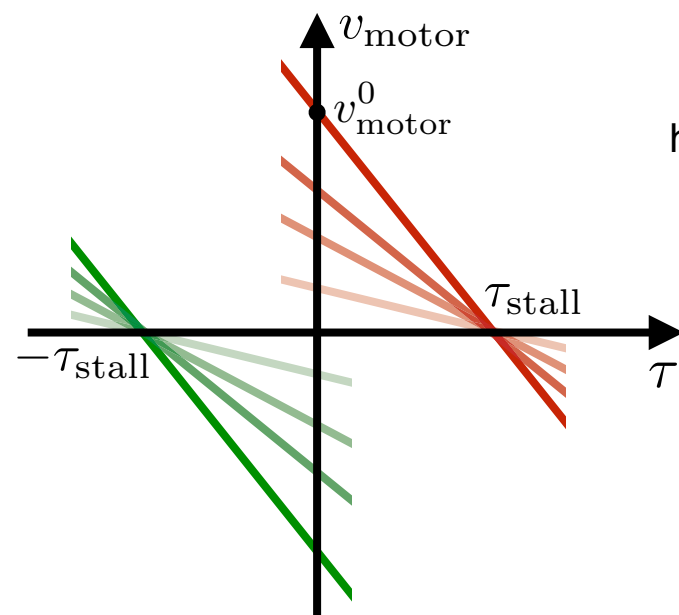
(iv) Mechanical interactions of the elastic, active pellicle with its environment

frictional forces

elastic penalty to bending

hydraulic forces

cellular pressure

contact forces

elastic penalty to deviations between the actual pellicle shear-rate and that imposed by motors: $v_{\mathrm{motor}}(s,t)/w$

b

c

(i) high hydraulic resistance

space

time

f1

f2

f3

f4

(ii) high wall friction

space

time

normalized flow rate

-1   0

h1

h2

h3

h4

d

high hydraulic resistance

high wall friction

f2

f3

f4

f1

h2

h3

h4

h1

Normalized cell velocity

Normalized capillary diameter
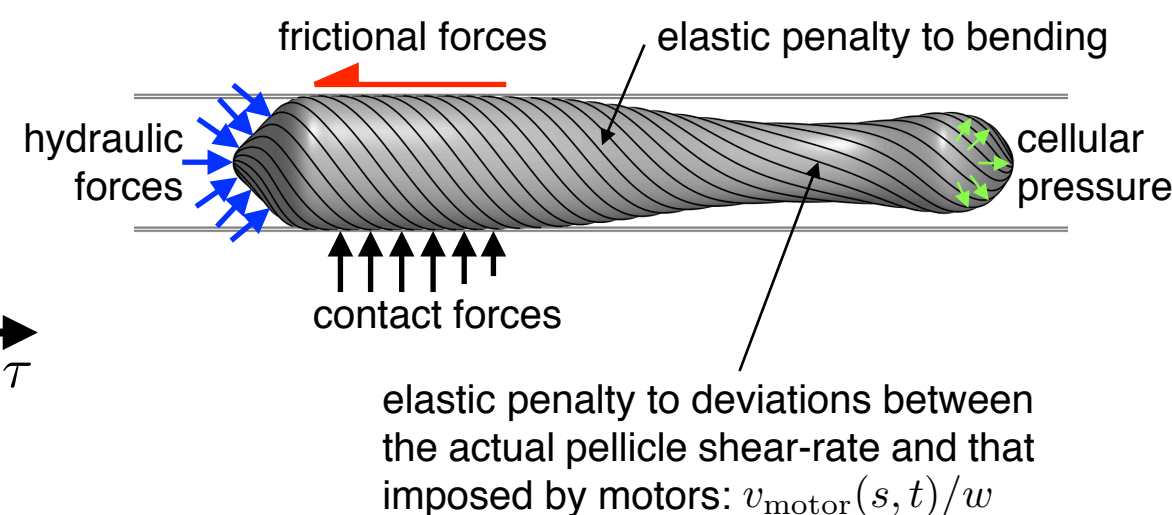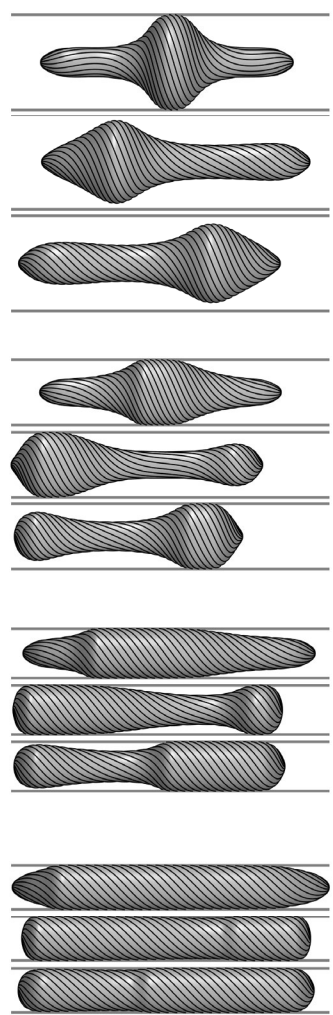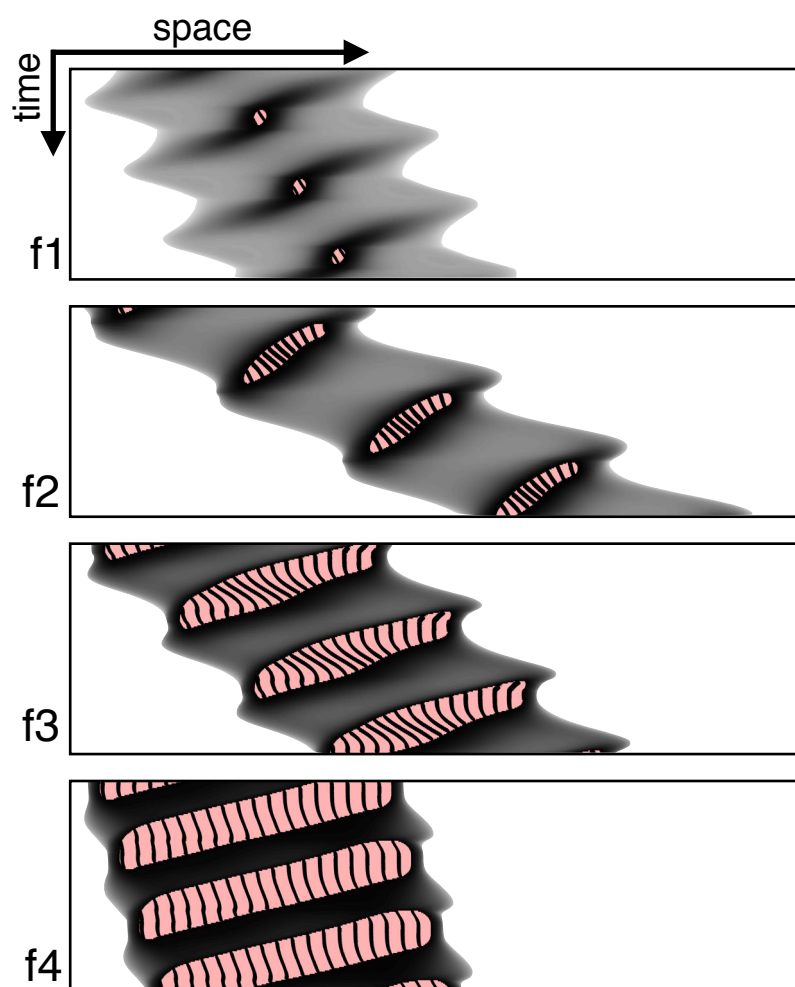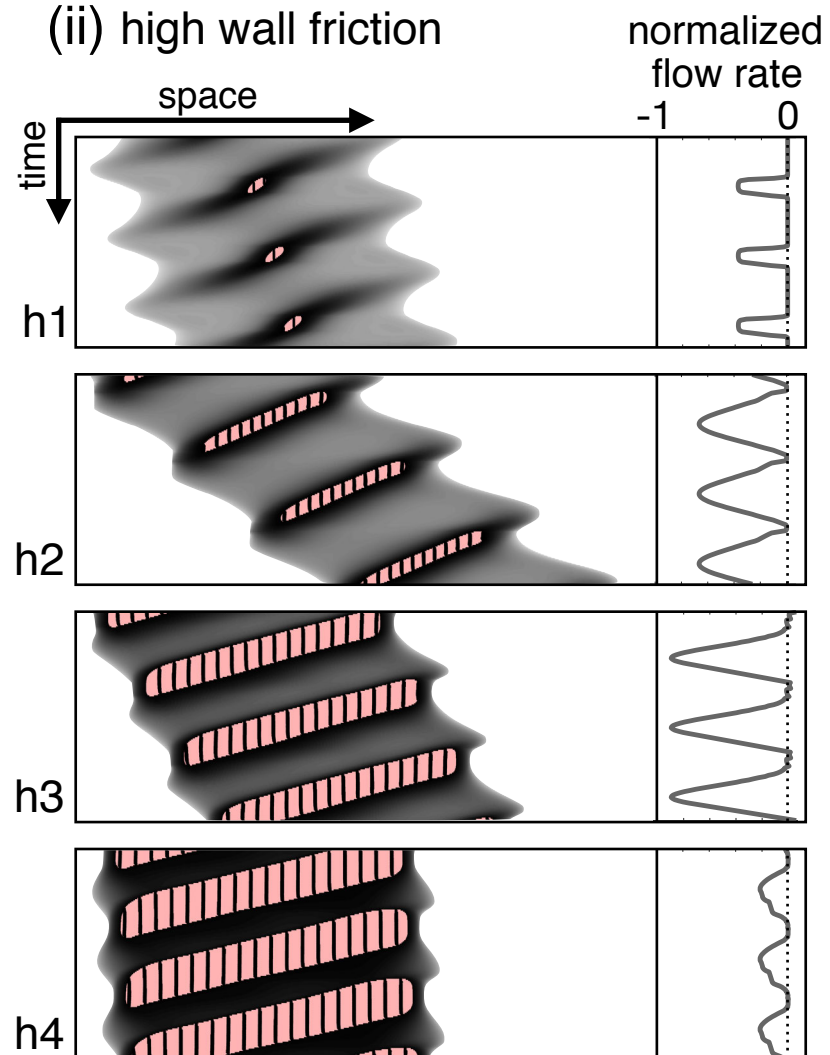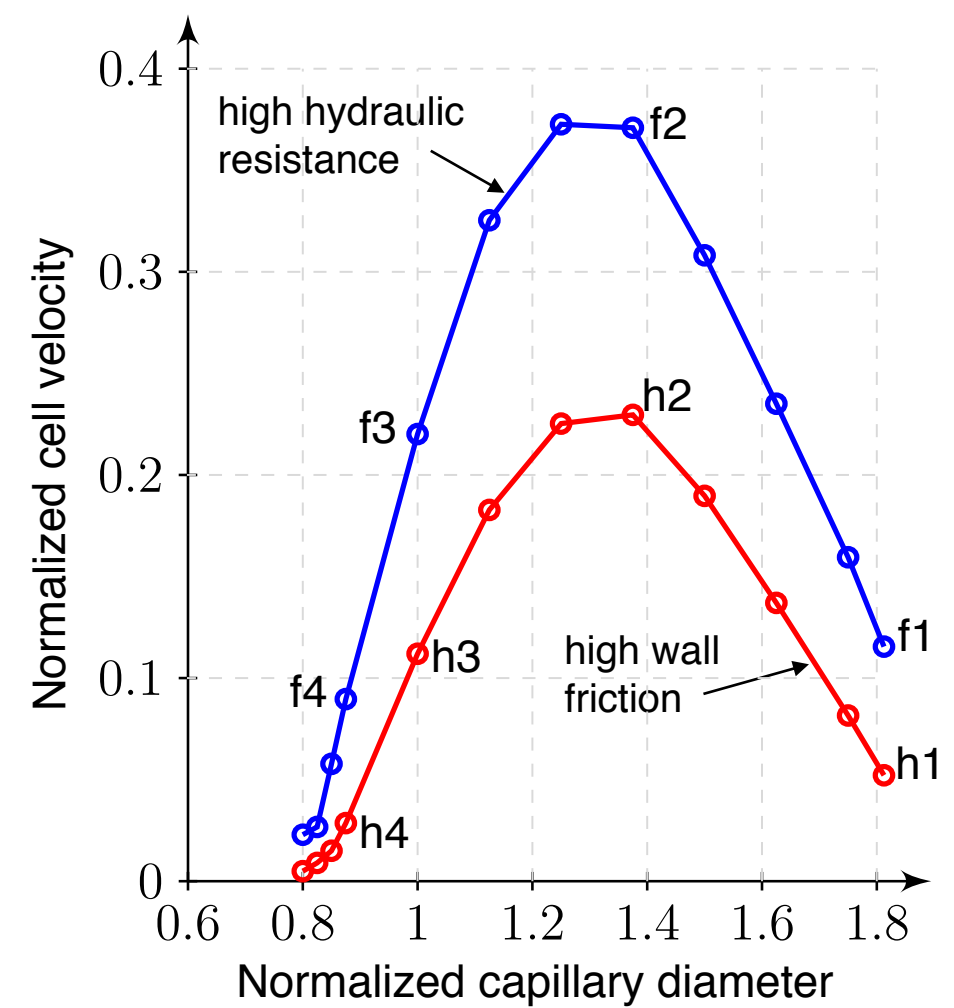
Supplementary information

Contents

Supplementary Note 1
Theory relating pellicle strip geometry and inter-strip sliding

We particularize to the observations in Fig. 1(b) a previously developed theory relating the sliding between adjacent strips and the pellicle configuration [7, 18]. We consider the deformation of a planar region of pellicle with initially straight strips as shown in Supplementary Fig. 1. Because in the experiments in Fig. 1(b) cells are sandwiched between glass plates, the deformation of the imaged region of pellicle is such that it remains planar. We describe it mathematically by the mapping $\boldsymbol{x}(u, v)$ from the plane to the plane, where v is a coordinate along the pellicle strips.
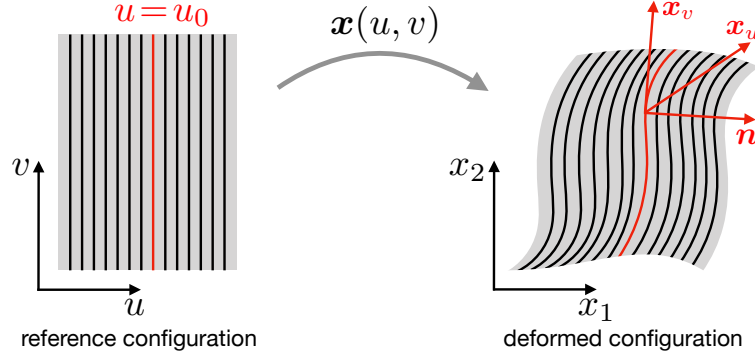
Supplementary figure 1: Sketch of the planar deformation of a region of pellicle. We consider an ideal reference configuration in which all pellicle strips are straight, which is deformed by the mapping $\boldsymbol{x}$.

According to the mechanism of deformation of the pellicle, this deformation is the result of a local shear deformation along the strips given by $\gamma(u, v)$. The relation between the deformation mapping $\boldsymbol{x}$ and the pellicle shear distribution γ is given by the relations [7, 18]

$$1 + \gamma^2 = \boldsymbol{x}_u \cdot \boldsymbol{x}_u, \tag{1}$$

$$1 = \boldsymbol{x}_v \cdot \boldsymbol{x}_v, \tag{2}$$

$$\gamma = \boldsymbol{x}_u \cdot \boldsymbol{x}_v, \tag{3}$$

where $\boldsymbol{x}_u$ and $\boldsymbol{x}_v$ denote the partial derivatives of $\boldsymbol{x}$ with respect to the coordinates u and v. Pellicle lines are given by $u = u_0 = \text{constant}$ in the reference configuration and by $\boldsymbol{x}(u_0, v)$ in the deformed configuration. Thus, the vector field $\boldsymbol{x}_v$ is tangential to deformed pellicle lines. Furthermore, Eq. (2) shows that this vector field has unit length, and thus $\boldsymbol{x}(u_0, v)$ is an arc-length parametrization of the deformed pellicle strip given by $u = u_0$ (pellicle strips do not stretch). Since v is the arc-length parameter, the signed curvature of pellicle strips κ is given by the relation [36]

$$\boldsymbol{x}_{vv} = \kappa \boldsymbol{n}, \tag{4}$$

where $\boldsymbol{n}$ is a unit vector field normal to the pellicle strips. An expression for the normal vector can be obtained by subtracting to $\boldsymbol{x}_u$ its projection along $\boldsymbol{x}_v$, see Supplementary Fig. 1,

$$\boldsymbol{n} = \boldsymbol{x}_u - (\boldsymbol{x}_u \cdot \boldsymbol{x}_v)\,\boldsymbol{x}_v = \boldsymbol{x}_u - \gamma \boldsymbol{x}_v, \tag{5}$$

where we have used Eq. (3). Note that $|\boldsymbol{n}|^2 = \boldsymbol{n} \cdot \boldsymbol{n} = \boldsymbol{x}_u \cdot \boldsymbol{x}_u - 2\gamma \boldsymbol{x}_u \cdot \boldsymbol{x}_v + \gamma^2 \boldsymbol{x}_v \cdot \boldsymbol{x}_v = 1$, where we have used Eqs. (1–3). We conclude that

$$\boldsymbol{x}_{vv} = \kappa\,(\boldsymbol{x}_u - \gamma \boldsymbol{x}_v)\,. \tag{6}$$

To find an alternative expression for the vector $\boldsymbol{x}_{vv}$, we express it in the basis formed by $\boldsymbol{x}_u$ and $\boldsymbol{x}_v$ as

$$\boldsymbol{x}_{vv} = a\boldsymbol{x}_u + b\boldsymbol{x}_v. \tag{7}$$

Differentiation of the Eq. (2) with respect to u and v leads to

$$0 = \boldsymbol{x}_v \cdot \boldsymbol{x}_{uv}, \tag{8}$$

$$0 = \boldsymbol{x}_v \cdot \boldsymbol{x}_{vv}. \tag{9}$$

Differentiation of the Eq. (3) with respect to v leads to

$$\gamma_v = \boldsymbol{x}_u \cdot \boldsymbol{x}_{vv} + \boldsymbol{x}_v \cdot \boldsymbol{x}_{uv} = \boldsymbol{x}_u \cdot \boldsymbol{x}_{vv}, \tag{10}$$

where we have used Eq. (8) in the second step. Thus, combining Eqs. (7, 9, 10) we find

$$\gamma_v = \boldsymbol{x}_u \cdot \boldsymbol{x}_{vv} = (1 + \gamma^2)a + \gamma b, \tag{11}$$

$$0 = \boldsymbol{x}_v \cdot \boldsymbol{x}_{vv} = \gamma a + b. \tag{12}$$

Inverting these relations, we find that $a = \gamma_v$ and $b = -\gamma\gamma_v$, and thus

$$\boldsymbol{x}_{vv} = \gamma_v \left(\boldsymbol{x}_u - \gamma\boldsymbol{x}_v \right). \tag{13}$$

Comparing this expression with Eq. (6), we conclude that

$$\gamma_v = \kappa, \tag{14}$$

which coincides with the expression in Fig. 1(d) denoting v by s.

To compute relative sliding displacements from this expression, we considered pellicle strips emanating from the anterior end (given by $s = 0$), where strips converge and cannot slide relative to each other, $\gamma(s = 0) = 0$. We then fitted spline curves to such strips and computed their curvature as a function of arc-length $\kappa(s)$ at selected time instants. The sliding displacement required to bend an initially straight strip to the observed configuration is then

$$w\gamma(s) = w \int_0^s \kappa(r) \, dr, \tag{15}$$

computed as the product of the shear strain and the width of a strip w.

Supplementary Note 2
Estimation of friction coefficient and hydraulic resistance in the capillary

Biological locomotion at microscopic scales is the result of forces exerted by the environment on the cell surface. For an *Euglena* cell under capillary confinement, these forces are exerted on the pellicle by the fluid in the capillary and by the capillary walls. Hydrodynamic forces are essentially those required to displace the column of water in the capillary as the cell moves. Since *Euglena* are not known to establish specific adhesions with substrates, we reasoned that the mechanical interaction with the capillary wall should include contact forces normal to it, and thus not directly contributing to propulsion, and tangential forces due to unspecific viscous friction and thus proportional to the sliding velocity, in agreement with previous reports on animal cells [24] and with the framework of hydration lubrication [37], which studies the rheological properties of thin aqueous interfaces such as those between cells and solid substrates.

To understand and quantify the forces experienced by a non-deforming cell moving under capillary confinement, we drove cells into the narrower sections of capillaries. Tapered glass capillaries of circular cross section were filled with a diluted solution of cells and of 1 μm polystyrene, fluorescent beads (~ 1.5 mg/mL from Life Technologies, catalog number F8823) in culture medium (CM) Eg. The capillaries were then fixed to the microscope stage by means of a custom made, 3d-printed holder and their inlet was connected to an external reservoir of CM. The holder was designed in such a way that the capillaries were positioned

between two 0.17 mm coverslips and immersed in CM. Starting from a state of hydrostatic equilibrium, lifting the external reservoir resulted in a controlled increase of the pressure (relative to the reference atmospheric pressure) at the capillary inlet, p_{in}, and in fluid flow within it. Eventually, a cell convected by the flow contacted the capillary wall and created a hydraulic seal. This condition was verified by the imaging of micro-beads diluted in the solution, whose velocity correlated with that of the cell and which stopped when cells became immobile, Supplementary Movie S7. Consequently, under these conditions cell velocity was a reporter of the flow rate in the capillary. Note that in a Poiseuille flow, beads can go faster or slower than the average flow velocity given by that of the cells.
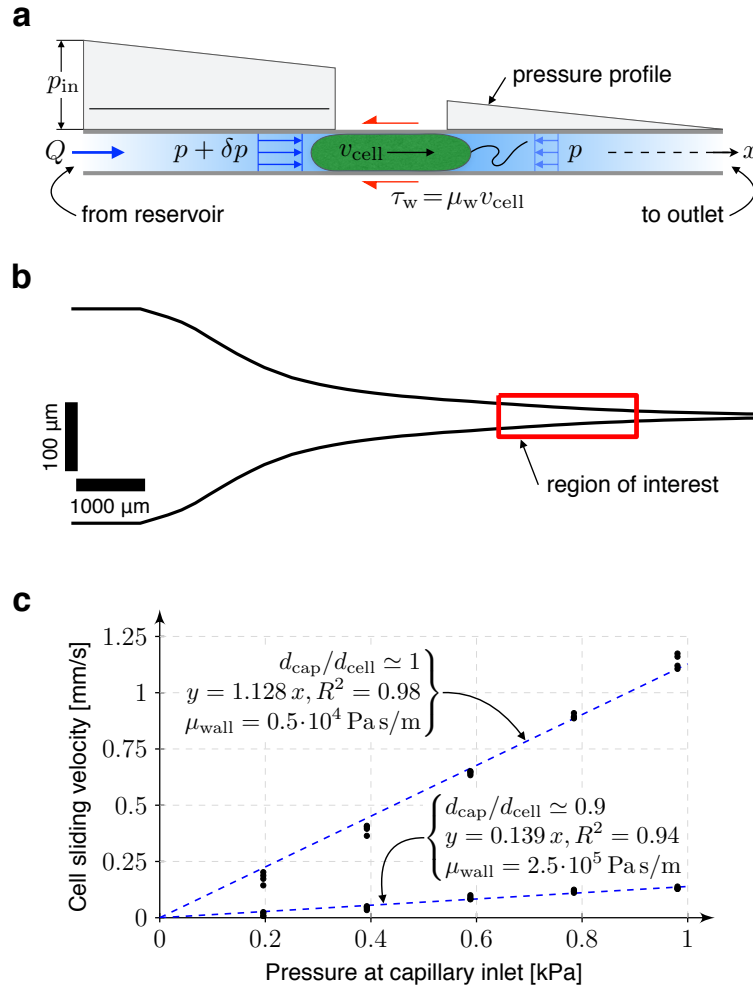
Supplementary figure 2: Estimation of friction coefficient and hydraulic resistance in the capillary. (a) Force balance for a confined cell moving in a capillary by a pressure difference. (b) profile of a typical pulled capillary. (c) Linear relation between the cell velocity and the applied pressure, allowing us to measure the friction coefficient μ_{wall}. We performed four measurements from the same sample for each condition (confinement and appalied pressure). We performed analogous measurements for other cells.

The cell motion along the capillary axis was recorded at 40 fps with a Basler digital camera (model acA2000-50gm) and an Olympus Plan N 10X objective (NA 0.25). Analysis of the micrographs allowed us to determine the cell position along the capillary x_{cell}, its radius, which coincides with the capillary radius at the cell position $r(x_{\text{cell}})$, the cell velocity v_{cell}, and the length of the contact area ℓ_{c}.

Inertia being negligible in these experiments, the net forces due to pressure differences across a cell δp and given by

$$F_{\text{fluid}} = \delta p \pi r^2, \tag{16}$$

4

had to be balanced by the frictional forces between the cell and the capillary, which we modeled as

$$F_{\text{wall}} = -2\pi r \ell_c \mu_{\text{wall}} v_{\text{cell}} \tag{17}$$

where μ_{wall} is a viscous friction coefficient linearly relating sliding velocity, which here coincides with the cell velocity, and the frictional force per unit area $\tau_{\text{wall}} = \mu_{\text{wall}} v_{\text{cell}}$, Supplementary Fig. 2(a). By balancing these two forces, we found

$$\delta p = \frac{2\ell_c}{r} \mu_{\text{wall}} v_{\text{cell}}. \tag{18}$$

The pressure jump across the cell δp could also be estimated with elementary hydrodynamics. Assuming a Poiseuille flow and small capillary taper ($dr/dx \ll 1$) leads to

$$\frac{dp}{dx} = -\frac{8\eta}{\pi r^4} Q, \tag{19}$$

where η is the dynamic viscosity of the solvent and $Q = \pi r^2 v_{\text{cell}}$ is the flow rate. The pressure difference across the cell, δp, was determined by integration of the equation above while accounting for the boundary conditions on pressure at inlet and outlet (where $p = 0$), leading to

$$\delta p = p_{\text{in}} - \frac{\zeta}{\pi} Q, \tag{20}$$

where

$$\zeta = 8\eta \left(\int_0^{x_{\text{cell}} - \ell_c/2} r^{-4} \, dx + \int_{x_{\text{cell}} + \ell_c/2}^{L} r^{-4} \, dx \right) \simeq 8\eta \int_0^L r^{-4} \, dx, \tag{21}$$

is the the hydraulic resistance and L the capillary length. We computed this quantity for the actual geometry of the capillaries as measured from the micrographs, Supplementary Fig. 2(b), obtaining $\zeta = 5 \cdot 10^{16}$ N s/m^5.

Equating the two expressions for δp, we obtained the following linear relation between cell velocity and pressure applied at the inlet

$$p_{\text{in}} = \left(\frac{2\ell_c}{r} \mu_{\text{wall}} + r^2 \zeta \right) v_{\text{cell}}. \tag{22}$$

Since the coefficient μ_{wall} could depend on the lateral confining pressure, we considered the possibility that it could be confinement-dependent. For this reason, μ_{wall} could be considered as constant in the equation above, provided that measurements were performed at a given position in the capillary x with radius $r(x)$. To test this relationship, we carried out tests for different values of p_{in} and measured cell velocity at specified positions (and thus specified degrees of confinement). Consistent with our model, we found a confinement-dependent linear relationship between inlet pressure and cell velocity, Supplementary Fig. 2(c), which allowed us to measure the ratio $p_{\text{in}}/v_{\text{cell}}$ and thereby the confinement-dependent friction coefficient μ_{wall}. Indeed, rearranging Eq. (22) we have

$$\mu_{\text{wall}} = \frac{r}{2\ell_c} \left(\frac{p_{\text{in}}}{v_{\text{cell}}} - r^2 \zeta \right). \tag{23}$$

Our measurements for the friction coefficient were in the range of $10^4 - 10^5$ Pa s/m, comparable to those reported between animal cells and PDMS channels [24].

Supplementary Note 3
Feasibility of flagellar locomotion in capillary confinement

From the typical speed of free-swimming cells, $v_{\text{free}} \simeq 68$ μm/s, and approximating their body geometry by prolate spheroids of semi-major and semi-minor axis $a \simeq 25$ μm and $b \simeq 4.5$ μm to compute the drag coefficient, we estimated the flagellar propulsive force to be

$$F_{\text{p}} = 6\pi\eta a v_{\text{free}} \chi(e) \simeq 10.9 \, \text{pN}, \tag{24}$$

where

$$\chi(e) = \frac{8e^3}{3[(1 + e^2)\log[(1 + e)/(1 - e)] - 2e]} \tag{25}$$

is a coefficient accounting for the spheroid eccentricity, $e = [1 - (b/a)^2]^{1/2}$ [38].

Assuming that a cell could exert the same propulsive force in capillary confinement, in order to move forward it would need to overcome the hydraulic resistive force F_{fluid} required to move the column of water in the capillary and the frictional force F_{wall}. Adapting the model of the Supplementary Note 2, we have

$$F_{\text{fluid}} = -8\pi\eta r^4 v_{\text{cell}} \int_0^L r^{-4}\,dx = -\pi\zeta r^4 v_{\text{cell}}, \tag{26}$$

where $\zeta \simeq 5 \cdot 10^{16}$ N s/m^5 is defined in Eq. (21), and

$$F_{\text{wall}} = -2\pi r \ell_c \mu_{\text{wall}} v_{\text{cell}}. \tag{27}$$

Force balance during flagellar locomotion requires that $F_{\text{p}} + F_{\text{fluid}} + F_{\text{wall}} = 0$, and thus

$$F_{\text{p}} = -F_{\text{fluid}} - F_{\text{wall}} = \pi\left(\zeta r^4 + 2r\ell_c\mu_{\text{wall}}\right) v_{\text{cell}}, \tag{28}$$

which allows us to estimate the velocity at which a cell would move in capillary confinement while propelled by flagella. We considered a first situation of moderate confinement ($d_{\text{cap}}/d_{\text{cell}} \approx 1$), with $r = 4.5\,\mu$m, $\ell_c = 10\,\mu$m and $\mu_{\text{wall}} = 0.5 \cdot 10^4$ Pa s/m, which led to $v_{\text{cell}} \sim 0.15\,\mu$m/s, about 10 times smaller that the crawling velocity by metaboly at this degree of confinement, Fig. 2(c). We then considered a more confined case with $r = 4\,\mu$m, $\ell_c = 30\,\mu$m and $\mu_{\text{wall}} = 2.5 \cdot 10^5$ Pa s/m, which led to $v_{\text{cell}} \sim 0.05\,\mu$m/s, about 20 times smaller that the crawling velocity by metaboly at this degree of confinement.

Supplementary Note 4
Theoretical model of the power phase of metaboly

During metaboly, a power phase corresponding to a bulge of fixed shape traveling along the body in direction opposite to that of the resulting crawling motion can be clearly identified, see Supplementary Movie 6 and Figs. 2 and 3. A simplified model of this process can be derived by assuming that the strips in the thinner cylindrical end sections are all aligned with the main body axis, and that the angle θ^* between strips in the bulge and that axis is constant in the region in contact with the capillary. We note that allowing strips in the thinner section of the cell body to be helical slightly complicates the mathematical expressions but does not fundamentally alter the conclusions. The transition between the wider cylindrical bulge, of radius r, and the thinner cylindrical end sections, of radius r_0, can be realized by modulating the pellicle shear from the maximal value γ^* at the bulge, and the reference value $\gamma = 0$ at the ends, provided that the transition region is sufficiently long [18]. The bulge is assumed to be in contact with the capillary walls in a region of length ℓ_c, establishing a hydraulic plug which does not allow transfer of fluid between the regions ahead of and behind the cell. See Fig. 3(b) and Supplementary Fig. 3 for an illustration. Elementary geometry shows that the radius of the slender part of the cell body, that of the bulge in contact with the capillary, and the angle θ^* follow the relation [18]

$$r_0 = r\cos\theta^*. \tag{29}$$

To analyze the kinematics and mechanics of this idealized gait, we define three frames of reference, the laboratory frame where the capillary is quiescent, whose origin is O, the frame of the cell fixed for instance at the leading edge of the cell (O_{tip}), and a frame attached to a fixed material point (O_{contact}) in the region of the bulge in contact with the wall, see Supplementary Fig. 3. We assume that the bulge is generated by a traveling localized profile of active shear given by $\gamma(s, t) = \bar{\gamma}(s - ct)$, where c is the velocity of the actuation pattern along the coordinate s describing arc-length of strips, Fig. 3(b). We adopt the convention

that all velocities are positive when they represent motions from left to right. Since we consider backward moving bulges, $c < 0$. As a result of this motion of the activation pattern, the bulge also moves backwards at velocity c in the frame of the cell. In the frame attached to O_{contact}, however, the bulge moves slower at velocity $c \cos \theta^*$ given the geometry of the bulge.

The other velocities characterizing the kinematics of the cell are

- the sliding velocity v_{s}, that is the velocity of O_{contact} relative to O,

- the velocity of O_{tip} relative to O_{contact}, dl/dt,

- the cell velocity v in the laboratory frame, that is the velocity of O_{tip} relative to O,

- the velocity of the bulge v_{b} in the laboratory frame (the velocity of the leading edge of the bulge relative to O),

- the average fluid velocity $v_{\text{f}} = Q/(\pi r^2)$ in the capillary at a small distance from the cell in the laboratory frame.
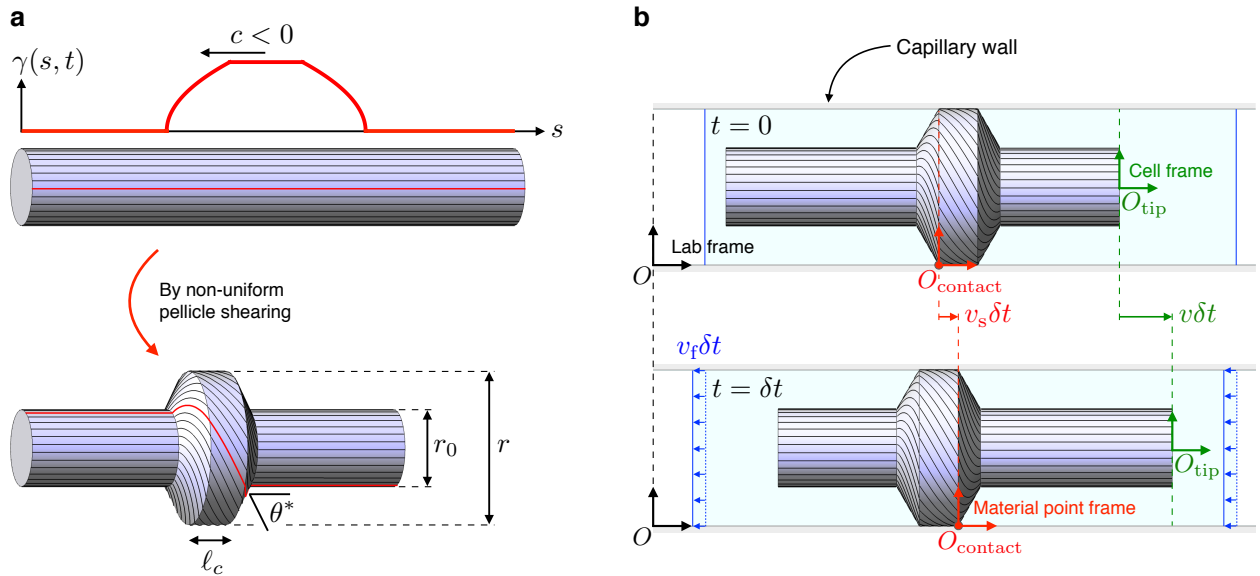
Supplementary figure 3: (a) Idealized model of the power phase of metaboly and (b) two snapshots of the resulting motion in a capillary to highlight the frames of reference relevant to the analysis and the three velocities v, v_{s}, and v_{f}.

We assume c to be given, and obtain the other five unknown velocities from the kinematics of the traveling bulge and force balance. The forces acting on the cell are the frictional force exerted by the wall, which depends on the velocity of points in the contact region relative to the capillary wall

$$F_{\text{wall}} = -2\pi r \ell_{\text{c}} \mu_{\text{wall}} v_{\text{s}} \,, \tag{30}$$

and the hydraulic force exerted by the fluid

$$F_{\text{fluid}} = -\alpha Q = -\alpha \pi r^2 v_{\text{f}} \,, \qquad \text{where} \quad \alpha = \zeta r^2 \,, \tag{31}$$

ζ is defined in (21), and the expression of F_{fluid} follows from (20) by assuming that inlet and outlet are at atmospheric pressure, $p_{\text{in}} = p_{\text{out}} = 0$. Force balance on the cell gives then

$$0 = F_{\text{wall}} + F_{\text{fluid}} \,. \tag{32}$$

Introducing the nondimensional parameter

$$\xi = \frac{2\mu_{\text{wall}}\ell_c}{\alpha r} \tag{33}$$

controlling the relative strength of friction and hydraulic resistance, force balance can be rewritten as

$$0 = \xi v_s + v_f . \tag{34}$$

From the previous definitions, we can express the velocity of the bulge in the laboratory frame in terms of its velocity relative to O_{contact} and the sliding velocity as

$$v_b = v_s + c \cos \theta^* . \tag{35}$$

Likewise, we can express the cell velocity relative to O as

$$v = v_s + \frac{dl}{dt} . \tag{36}$$

Furthermore, noting that the pellicle deformation mechanism locally preserves area, and thus the area of pellicle to the right (or left) of material point O_{contact} remains constant during the motion, we derive the following relation

$$0 = 2\pi(r - r_0)c \cos \theta^* + 2\pi r_0 \frac{dl}{dt} . \tag{37}$$

Finally, volume conservation of the fluid inside the capillary yields

$$\pi r^2 v_f = Q = \pi(r^2 - r_0^2)v_b + \pi r_0^2 v . \tag{38}$$

Solving the last five equations for the five unknown velocities we obtain

$$v_s = -\frac{1}{1 + \xi}(1 - \cos \theta^*) \cos \theta^* c , \tag{39}$$

$$v_f = \frac{\xi}{1 + \xi}(1 - \cos \theta^*) \cos \theta^* c , \tag{40}$$

$$v = -\left(1 + \frac{\cos \theta^*}{1 + \xi}\right)(1 - \cos \theta^*) c , \tag{41}$$

$$v_b = \frac{\cos \theta^* + \xi}{1 + \xi} \cos \theta^* c , \tag{42}$$

and

$$\frac{dl}{dt} = -(1 - \cos \theta^*) c . \tag{43}$$

In the limit of vanishing hydrodynamic resistance relative to the wall friction, $\xi \to +\infty$, we obtain

$$v = -(1 - \cos \theta^*)c , \qquad v_s = 0 , \qquad v_f = (1 - \cos \theta^*) \cos \theta^* c . \tag{44}$$

In the opposite limit of vanishing wall friction relative to hydraulic resistance, $\xi \to 0$, we obtain instead

$$v = -\left(1 - \cos^2 \theta^*\right) c , \qquad v_s = -(1 - \cos \theta^*) \cos \theta^* c , \qquad v_f = 0 . \tag{45}$$

It is easy to see that, in the general case, the cell, sliding, and fluid velocities are intermediate between those of the two extreme situations.

Supplementary Note 5
Computational model of confined crawling

Setup

We describe mathematically the pellicle of euglenids as a deformable surface and focus on axisymmetric cells. We consider a reference configuration of the cell given by a surface Γ described by a parametrization of its generating curve $\{\rho_0(u), z_0(u)\}$, $u \in [0, 1]$, not necessarily parametrized by arc-length. In this reference configuration, the pellicle strips are meridians of the axisymmetric surface, see Supplementary Fig. 4. A general deformed configuration of the cell at time t under the assumption of axisymmetry is defined by the deformed generating curve and the azimuthal angle displacement, $\{\rho(u, t), z(u, t), \psi(u, t)\}$. We denote space derivatives by ρ' and time derivatives by $\dot{\rho}$.
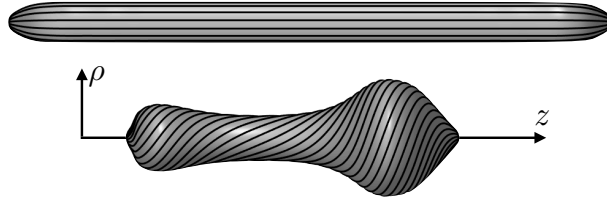
Supplementary figure 4: Reference pellicle surface Γ (top) and an axisymmetric deformed shape of the reference pellicle resulting from a nonuniform pellicle shear distribution (bottom).

The pellicle is an active surface, capable of undergoing simple shear along a Lagrangian direction given by the strips under the action of molecular motors. We denote the pellicle shear field relative to the reference configuration by $\gamma(u, t)$. Shape changes are the result of this actively generated deformation. The precise connection between deformation and pellicle shear can be established by noting that the (Cauchy-Green) deformation tensor of the surface can be expressed either as [7, 18]

$$C = \begin{bmatrix} \frac{\rho'^2 + z'^2 + \rho^2 \psi'^2}{a_0^2} & \frac{\rho^2 \psi'}{\rho_0 a_0} \\ \frac{\rho^2 \psi'}{\rho_0 a_0} & \left(\frac{\rho}{\rho_0}\right)^2 \end{bmatrix}, \tag{46}$$

where $a_0^2 = \rho_0'^2 + z_0'^2$, or as

$$\bar{C} = \begin{bmatrix} 1 & \gamma \\ \gamma & 1 + \gamma^2 \end{bmatrix}. \tag{47}$$

By equating these two forms of the same physical quantity, we obtain a set of algebraic and differential equations, which for instance allow us to compute $\{\rho(u, t), z(u, t), \psi(u, t)\}$ given the internal actuation $\gamma(u, t)$.

While this geometric approach is very powerful to understand the pellicle kinematics, it has limitations in the present context. First, the resulting equations do not always admit solutions. If the pellicle shear γ is too large or has very sharp variations, as made precise elsewhere [18], it may not be "embeddable", meaning that there exist no geometric realization of the pellicle having $\bar{C}$ as its deformation tensor. A way to make this set of kinematic relations more flexible, and also more physical, is to allow for some stretching of the surface, and elastically penalize deviations between C and $\bar{C}$ as described below. Another limitation of trying to prescribe $\gamma(u, t)$ directly is that, if an euglenid is performing metaboly in the presence of constraints such as the wall of a capillary, then the reaction forces associated with the constraints will oppose the action of the molecular motors and could even stall them. For this reason, rather than imposing the pellicle shear $\gamma(u, t)$, in the present model we impose a biological activity creating forces conjugate to pellicle sliding. We will then obtain $\gamma(u, t)$, now an unknown, as the result of balancing the externally applied forces on the motors with those being actively generated.

9

Model ingredients

To model the mechanics depicted in Fig. 4(a), which couple elasticity, dissipative mechanisms, constraints and active power input, we resort to Onsager's variational principle [39, 40], which, given the enumeration of the elastic and dissipation potentials describing the different physical mechanisms, provides a systematic tool to derive the governing mechanical equations by minimizing the Rayleighian functional. In this systematic modeling approach, it is important to formalize the state of the system, which here is given by the deformation of the pellicle and the actual pellicle shear distribution:

$$X(u, t) = \{\rho(u, t), z(u, t), \psi(u, t), \gamma(u, t)\}, \quad u \in [0, 1], t \geq 0.$$

We will derive equations to find the dynamics of these state variables.

Elastic energy

To account for the elastic in-plane stretchability of the pellicle and without attempting to describe in detail the possibly anisotropic mechanical properties of the pellicle, we consider a Kirchhoff-Saint Venant energy, which locally penalizes deviations between the actual deformation and that given by $\gamma(u, t)$, along with a Helfrich energy contribution to elastically penalize curvature

$$
\begin{aligned}
E_{\text{elastic}}[\rho, z, \psi, \gamma] =& \frac{Y}{2} \int_{\Gamma} |C - \bar{C}|^2 \, dS_0 + \frac{D}{2} \int_{\Gamma} H^2 \, dS_0 \\
=& \frac{Y}{2} \int_{\Gamma} \left[\left(\frac{\rho'^2 + z'^2 + \rho^2 \psi'^2}{a_0^2} - 1 \right)^2 + 2 \left(\frac{\rho^2 \psi'}{\rho_0 a_0} - \gamma \right)^2 + \left(\left(\frac{\rho}{\rho_0} \right)^2 - 1 - \gamma^2 \right)^2 \right] dS_0 \\
&+ \frac{D}{2} \int_{\Gamma} H^2 \, dS_0,
\end{aligned}
$$

where Y is the stretching modulus, D is a bending modulus, H is the mean curvature, and $dS_0 = 2\pi\rho_0 a_0 du$. Note that, because the pellicle surface is largely inextensible, dS_0 is very close to dS and the last term closely approximates the usual Helfrich functional used to model lipid membranes.

Volume conservation

At the typical time-scales of metaboly, our observations suggest that cells can be considered as incompressible. Without attempting to model the active and passive processes leading to cell volume regulation, we penalize volume variations with respect to a target volume $\bar{V}$ by

$$E_{\text{volume}}[\rho, z] = \frac{K}{2} \left(V[\rho, z] - \bar{V} \right)^2,$$

where $V[\rho, z]$ is the cell volume, depending only on the parametrization of the generating curve, and K is a parameter large enough to control cell volume variations within a few percent.

Contact with a capillary wall

We model the contact interaction with a capillary wall with a potential $\mathcal{V}(\rho)$ that becomes repulsive when $\rho \geq r$, the radius of the capillary. Here, we consider

$$
\mathcal{V}(\rho) = \begin{cases} 0 & \text{if } \rho < r \\ \dfrac{k}{p} \left(\dfrac{\rho - r}{\delta} \right)^p & \text{if } \rho \geq r \end{cases}
$$

where δ is the "thickness" of the interaction. We take $\delta \ll r$, $p = 3$, and the parameter k is large enough so that the maximum cell radius only exceeds r by a few percent. The resulting energy functional is

$$E_{\text{contact}}[\rho] = \int_{\Gamma} \mathcal{V}(\rho) \, dS_0.$$

10
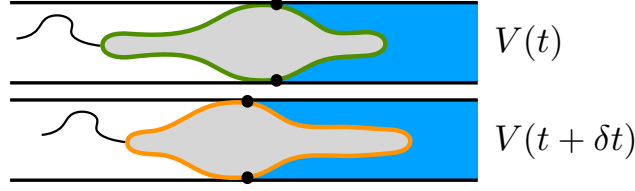
Supplementary figure 5: Calculation of the flow rate Q by comparing between time instants the volume of fluid at either side of the hydraulic plug delimited by the cell-wall contact.

Friction with the capillary wall

In agreement with previous related studies [24, 37], we assume that the rheology of the frictional interaction at the cell-capillary interface is viscous and linearly dependent on the normal pressure. Thus, the frictional traction is proportional to the relative sliding velocity, whose longitudinal and azimuthal components are $\dot{z}$ and $\rho\dot{\psi}$, with a coefficient μ_{wall} proportional to the normal pressure $\mathcal{V}'(\rho)$ and given by $\mu_{\text{wall}} = \bar{\mu}\mathcal{V}'(\rho)$. Thus, we can write the corresponding dissipation potential as

$$W_{\text{wall}}[\dot{z}, \dot{\psi}; \rho] = \int_{\Gamma} \frac{\bar{\mu}\mathcal{V}'(\rho)}{2}\left[\dot{z}^2 + (\rho\dot{\psi})^2\right] dS_0.$$

Note that at the locations where $\rho < r$, the normal pressure is zero and there is no frictional interaction. The longitudinal and azimuthal frictional tractions are given by

$$t_z = \frac{\delta W_{\text{wall}}}{\delta \dot{z}} = \mu\mathcal{V}'(\rho)\dot{z}, \qquad t_{\psi} = \frac{\delta W_{\text{wall}}}{\delta(\rho\dot{\psi})} = \mu\mathcal{V}'(\rho)\rho\dot{\psi}.$$

Hydraulic resistance

As the cells move in capillary confinement, they perturb the viscous fluid around them and dissipate energy. We can distinguish between local flows around the shape-changing cells and induced flow rates along the water column in the capillary. A direct scaling argument shows that the latter should be dominant in setting fluid forces onto the cell, and for this reason we only consider the viscous dissipation due to the induced flow rate in the capillary. Recalling the expression for F_{fluid} in Supplementary Note 4, the associated dissipation potential is

$$W_{\text{fluid}}[\dot{\rho}, \dot{z}; \rho, z] = \frac{\zeta}{2\pi}Q^2.$$

Since confined cells act as hydraulic plugs and are nearly incompressible, the flow rate Q can be computed as the rate of change of volume on either side of the cell-wall contact, see Supplementary Fig. 5. This volume depends on ρ and z, and therefore its rate is a linear functional of $\dot{\rho}$ and $\dot{z}$.

Motor activity

Models for molecular motors relate forces to velocities. In the present context, the "force" is a shear force per unit length along the strip direction, denoted by τ, opposing motor activity. The "velocity" is the sliding velocity between adjacent strips v_{motor}, obtained as pellicle shear rate times the strip width, $v_{\text{motor}} = w\dot{\gamma}$. In the absence of precise information about the nature, arrangement and constitutive relation of the motors powering the pellicle, we adopt an affine relation between v_{motor} and τ, Fig. 4(a)iii [30, 31]. This affine relation is characterized by a force-free velocity v_{motor}^0 and by a stall force τ_{stall}. To model motor activation, we assume that v_{motor}^0 is modulated in space and time, consistent with a control of the rate of ATP hydrolysis by the local calcium concentration. We further assume that the space-time pattern of activation $v_{\text{motor}}^0(s, t)$, Fig. 4(a)ii, is a time-periodic given function consistent with the shape dynamics of metaboly in the absence

11

of confinement [7], which can switch sign, and that the magnitude of the stall force τ_{stall} remains constant. Such a model can be mathematically expressed as

$$v_{\text{motor}} = v_{\text{motor}}^0 \left[1 - \left(\text{sign } v_{\text{motor}}^0 \right) \frac{\tau}{\tau_{\text{stall}}} \right],$$

or inverting this relation as

$$\tau = \left(\text{sign } v_{\text{motor}}^0 \right) \tau_{\text{stall}} \left(1 - \frac{v_{\text{motor}}}{v_{\text{motor}}^0} \right). \tag{48}$$

These equations show that for a given force τ and when motors are barely activated (very small v_{motor}^0), then the sliding velocity will also be very small, consistent with the notion that inactive motors remain in a bound state as in the flagellar axoneme [17]. In fact, in the limit $v_{\text{motor}}^0 = 0$, the force-velocity relation becomes the constraint $v_{\text{motor}} = 0$ and τ the corresponding Lagrange multiplier.

The constitutive model in Eq. (48) can be derived from an activity potential (a power per unit length) $a(v_{\text{motor}}, v_{\text{motor}}^0)$ as

$$\tau = -\frac{\partial a}{\partial v_{\text{motor}}}$$

with

$$a(v_{\text{motor}}, v_{\text{motor}}^0) = \left(\text{sign } v_{\text{motor}}^0 \right) \tau_{\text{stall}} \left(\frac{v_{\text{motor}}^2}{v_{\text{motor}}^0} - v_{\text{motor}} \right).$$

This activity potential is quadratic and convex for any value of v_{motor}^0, and it is minimized when $v_{\text{motor}} = v_{\text{motor}}^0$, which will only be realized when the net force along the motor system due to other physical mechanisms vanish. Thus, within the variational modeling approach adopted here, the activity of the molecular motors can be understood in terms of a dissipation potential whose minimizer is biased biologically. Recalling the relation between sliding velocity v_{motor} and pellicle shear rate $\dot{\gamma}$, the total activity potential over the entire pellicle is then given by

$$W_{\text{motor}}[\dot{\gamma}; v_{\text{motor}}^0] = \int_\Gamma \frac{1}{w} a(w\dot{\gamma}, v_{\text{motor}}^0) \, dS_0,$$

where w is the strip width.

Rayleighian and governing equations

Collecting all energy contributions, we have

$$E(X) = E_{\text{elastic}}[\rho, z, \psi, \gamma] + E_{\text{volume}}[\rho, z] + E_{\text{contact}}[\rho].$$

Therefore, the rate of change of energy can be computed from the functional derivative of E

$$\dot{E} = \frac{\delta E}{\delta X}(X) \cdot \dot{X} = \delta E(\dot{X}; X).$$

We also collect all dissipative/active contributions in

$$W(\dot{X}; X, t) = W_{\text{wall}}[\dot{z}, \dot{\psi}; \rho] + W_{\text{fluid}}[\dot{\rho}, \dot{z}; \rho, z] + W_{\text{motor}}[\dot{\gamma}; v_{\text{motor}}^0].$$

We then form the Rayleighian of the system as [39, 40]

$$R(\dot{X}; X, t) = \frac{\delta E}{\delta X}(X) \cdot \dot{X} + W(\dot{X}; X, t).$$

The dynamics of the system is then given by the minimization of the Rayleighian with respect to $\dot{X}$

$$\dot{X} = \arg \min_{\dot{X}} R(\dot{X}; X, t),$$

12

subject to geometric boundary conditions such as $\rho(0,t) = \rho(1,t) = z'(0,t) = z'(1,t) = 0$. The stationarity conditions $\delta_{\dot{X}} R = 0$ provide a system of nonlinear partial differential equations governing the time evolution of the system. Stationarity conditions with respect to the deformation $\{\rho, z, \psi\}$, that is $\delta_{\dot{\rho}} R = \delta_{\dot{z}} R = \delta_{\dot{\psi}} R = 0$, provide the mechanical equilibrium equations in the radial, longitudinal and azimuthal directions, balancing in-plane and bending elastic stresses, contact and frictional forces, the cell pressure resulting from the volume penalty and the hydrodynamic resistance. On the other hand, $\delta_{\dot{\gamma}} R = 0$ provides a statement of balance between actively generated forces at the pellicle strips and the forces acting externally on the motor system.

Force balance along the capillary axis

As a particular case, global force balance along the capillary axis can be obtained by equating to zero the variation of the Rayleighian with respect to a rigid motion along z,

$$0 = \left.\frac{d}{d\varepsilon}\right|_{\varepsilon=0} R(\dot{\rho}, \dot{z} + \varepsilon, \dot{\psi}, \dot{\gamma}; X).$$

Since all energetic contributions and the activity potential are invariant with respect to rigid body motions, this equation leads to only two contributions balancing the frictional force with the wall and the hydraulic force

$$0 = \bar{\mu} \int_{\Gamma} \mathcal{V}'(\rho)\dot{z} \, dS_0 + \zeta r^2 Q,$$

where the first term is the integral over the surface of the frictional traction t_z and the second term is F_{fluid}.

In the limit of large frictional coupling relative to the hydraulic resistance, this equations becomes

$$0 = \int_{\Gamma} \mathcal{V}'(\rho)\dot{z} \, dS_0,$$

which when divided by the net pressure force $\int_{\Gamma} \mathcal{V}'(\rho) \, dS_0$ can be interpreted as the average pellicle-wall sliding velocity in the contact region. Thus, we recover in this limit the no-sliding constraint, which determines the cell velocity independently of the parameter $\bar{\mu}$. In the limit of small frictional coupling relative to the hydraulic resistance, force balance becomes $Q = 0$, which determines the cell velocity independently of ζ and r.

Numerical discretization

The variational structure of the statement governing the dynamics of the system can be exploited computationally to formulate time-incremental minimization problems to advance in time. This results in nonlinearly stable implicit time-stepping schemes for the dynamics, which are very robust and efficient when combined with gradient-based optimization algorithms.

Suppose we consider discrete time-instants (t^n, $n = 0, 1, \dots$) at which we will approximate the time evolution. Suppose that we know the state of the system X^n at time t^n. Using for instance a simple backward-Euler scheme, we can approximate the time-continuos Rayleighian as

$$\frac{E(X^{n+1}) - E(X^n)}{t^{n+1} - t^n} + W\left(\frac{X^{n+1} - X^n}{t^{n+1} - t^n}; X^{n+1}, t^{n+1}\right)$$

and minimize it with respect to X^{n+1} to find the new state at time t^{n+1}. Since in this minimization $E(X^n)$ is a constant, we can rewrite the time-discrete Rayleighian as

$$R_{\Delta t}(X, X^n, t^{n+1}) = E(X) + \Delta t W\left(\frac{X - X^n}{\Delta t}; X, t^{n+1}\right)$$

where we have introduced the shorthand notation $\Delta t = t^{n+1} - t^n$. The time-stepping algorithm is then given by the time-incremental minimization principle

$$X^{n+1} = \arg \min_X R_{\Delta t}(X, X^n, t^{n+1}). \tag{49}$$

Having a time-discrete principle to derive the dynamics, we discretize all four unknown fields in space using a finite element expansion of the form

$$X(u, t) = \sum_I X_I(t) N_I(u), \quad \text{where} \quad X_I(t) = \{r_I(t), z_I(t), \psi_I(t), \gamma_I(t)\},$$

and where $N_I(u)$ are B-spline basis functions (cubic B-Splines in our calculations). The high degree of continuity of the B-Spline basis functions is required to deal with the bending elastic energy, which involves the mean curvature and hence second derivatives of the curve parametrization. Plugging this representation into $R_{\Delta t}(X, X^n, t^{n+1})$, Eq. (49) becomes an algebraic minimization problem that can be solved efficiently with gradient-based methods. The calculation of the gradient of the objective function is explicit and follows from the chain rule. Integrals are approximated using Gaussian quadrature in the knot spans of the B-Splines.

Selection of model parameters

The model parameters not related to capillary confinement are the pellicle stretching modulus Y, its bending modulus D, the cell compressibility modulus K, the space-time pattern of actuation $v^0_{\text{motor}}(s, t)$ and the stall force per unit length τ_{stall}. Since a mechanical and biophysical characterization of the pellicle is lacking, we performed rough estimations of these parameters. Our results, however, are largely insensitive to these choices as discussed below.

The stretching modulus was computed assuming a Young's modulus for the pellicle material of about 10 MPa, typical of proteinaceous materials, and multiplying it by a nominal thickness of 40 nm, resulting in $Y = 400$ nN/μm. Taking into account the geometry of cross-sections of the strips [1], we estimated the bending modulus as $D = 5$ nN·μm, about 100 times higher than that of a lipid bilayer.

As discussed in the main text, $v^0_{\text{motor}}(s, t)$ was inferred from the shape dynamics of unconfined cells [7], with a maximum sliding velocity of about $v_{\text{max}} = 0.5$ μm/s. To estimate τ_{stall}, we reasoned that, with our affine force-velocity relation, the maximum power generated per unit length in a pellicle strip interface is $v_{\text{max}} \tau_{\text{stall}}/4$. If we denote by ϕ the number of motors per unit length, we can estimate the maximum power required from a single motor protein as

$$P = \frac{v_{\text{max}} \tau_{\text{stall}}}{4\phi}.$$

The typical step length for motors running along microtubules is $\delta = 8$ nm, for which they hydrolyze a single ATP molecule. Assuming that 50% of the chemical energy is converted into mechanical energy, about $\Delta G = 40$ pN nm can be extracted per step. Thus, at maximum sliding velocity, the mechanical power produced by a single molecular motor is about

$$P = \frac{\Delta G v_{\text{max}}}{\delta}.$$

Equating these two expressions, we obtain

$$\tau_{\text{stall}} = \frac{4\phi \Delta G}{\delta}.$$

Assuming that motors bridge a pair of microtubules across the interface between adjacent strips, and that ϕ is one motor per 25 nm as in the axoneme, we find that $\tau_{\text{stall}} \approx 1$ nN/μm.

With these parameters and adjusting the compressibility modulus K so that cell volume variations are below 1%, the model reaches a limit cycle that very closely resembles metaboly in the absence of confinement, with total area changes below 2%. If Y is reduced, then area changes progressively become larger and become inconsistent with our observations. If D is reduced by an order of magnitude, then the pellicle exhibits buckling events during the gait, characterized by sudden shape transitions, not observed in our experiments. If D is increased by an order of magnitude, then the shape changes are smeared by the energetic cost of bending the pellicle and the bulge cannot adopt the sharp features observed experimentally.

When placed in capillary confinement, the thickness δ and stiffness k of the repulsive contact potential are adjusted so that the pellicle surface moves beyond the nominal capillary radius by less than 2%.

As discussed above, in the limit of high friction, the results do not depend on $\bar{\mu}$. Analogously, in the limit of high hydraulic resistance, the results do not depend on ζ. We analyzed the competition between friction and hydraulic resistance by choosing the friction coefficient so that $\mu_{\text{wall}} = \bar{\mu}\mathcal{V}'(\rho)$ agrees with our measurements reported in Supplementary Note 2, and evaluating ζ for our capillary geometry. We found that the results closely followed the limit of high hydraulic resistance, in agreement with the results reported in Fig. 3.

Supplementary Note 6
Confined metaboly in *Distigma proteus* and *Peranema trichophorum*

To test the generality of our observations, we first examined *Distigma proteus*, a primary osmotrophic species thought to have a phagotropic ancestor and exhibiting pronounced metaboly. We found that these cells swam using their flagella when unconfined. As for *Euglena gracilis*, confinement between two plates triggered non-reciprocal peristaltic cell deformations, which allowed *Distigma* cells to crawl at speeds of about 0.41 ± 0.04 body lengths per cycle (SEM, n=4), see Supplementary Movie S14. We then examined *Peranema trichophorum*, a voracious phagotroph known to engulf very large prey thanks to cell body deformations. In the absence of confinement, these cells glided on the substrate thanks to movements of the tip of their visible propulsive flagellum [41]. During gliding, they occasionally changed shape, including bending of their body in a coordinated movement that also involved a change in the gait of the flagellum and that resulted in sharp turns of their trajectory [42]. Under high confinement between two glass plates, *Peranema* cells were not able to glide and consistently developed periodic shape changes, see Supplementary Movie S15. However, in contrast with those of *Euglena* or *Distigma* cells, these shape changes were less specific, largely reciprocal, and did not accomplish significant net motion.

Thus, a minimal examination of metaboly across euglenids suggests that species endowed with a deformable pellicle can operate this motile machinery in various ways, possibly accomplishing different functions. *Peranema* cells, phagotrophs as the ancestor of all cells examined here, use it to engulf large objects and to bend their body during turns while gliding. *Euglena* and *Distigma* cells, which do not use metaboly for phagotropy, develop a remarkably non-reciprocal version of metaboly under confinement, which enables fast and versatile crawling. Our computational model shows that these different modes of operation of the pellicle only require different space-time activation patterns, which suggests that functional innovations of the pellicle do not require modifications of the complex cortical system but rather changes in the signaling networks that determine pellicle activation in space and time. The broader implications of this observation will be the subject of future studies.

Captions of Supplementary Movies

Supplementary Movie S1: Video recordings of *Euglena gracilis* between glass slides separated by a spacer of thickness $\sim 80\,\mu\text{m}$. In dilute cultures (left), cells exhibit flagellar swimming without cell shape changes. In crowded cultures (right), cells display a variety of behaviors, including flagellar swimming, cell rounding and spinning, and large amplitude periodic cell body deformations typical of metaboly.

Supplementary Movies S2 and S3: *Euglena gracilis* cells exhibiting metaboly and directed motion in the anterior-to-posterior direction while confined between glass slides. Observation using brightfield reflected light microscopy reveals the reconfigurations of the striated cell envelope concomitant with cell body deformations in the plane of the glass slide. The separation between the slides is $\sim 6\,\mu\text{m}$ and $\sim 4\,\mu\text{m}$ for Supplementary Movie S2 and S3, respectively.

Supplementary Movie S4: Video recordings of *Euglena gracilis* in tapered capillaries. Cells swimming into tapered capillaries transition from flagellar swimming (top left) to developing large amplitude shape excursions (top right), including rounding (bottom left). When confined in capillary diameters smaller than about twice the free-swimming cell diameter, most cells develop the prototypical peristaltic cell body deformations of metaboly (bottom right).

Supplementary Movie S5: *Euglena gracilis* cell confined in a glass capillary and imaged using brightfield reflected light microscopy. Rounding of the cell body, as determined by the reconfigurations of the pellicle strips, allows the cell to switch its orientation. The microscope was intermittently focused at the pellicle-capillary interface to visualize the pellicle and at the capillary axis to visualize cell shape.

Supplementary Movie S6: Video recordings of *Euglena gracilis* exhibiting metaboly and directed motion in tapered capillaries under increasing confinement, as quantified by ratio of $d_{\mathrm{cap}}/d_{\mathrm{cell}}$, along with kymographs relative to the capillary axis. The movie shows that crawling by metaboly is effective up to very large degree of confinement.

Supplementary Movie S7: Video recordings of *Euglena gracilis* not exhibiting body deformations and acting as hydraulic plugs driven by a known pressure difference, p_{in}, of increasing magnitude between the capillary extremities. Data from these experiments allowed us to quantify a viscous and confinement-dependent friction between cells and the capillary walls.

Supplementary Movie S8: Video recordings of *Euglena* cells stuck in a glass capillary and beating their anterior flagellum.

Supplementary Movie S9: Results from the idealized model for the power phase of metaboly in the limit of infinite wall friction relative to hydraulic resistance (top), in the limit of zero wall friction relative to hydraulic resistance (bottom), and for an intermediate case where hydraulic propulsive forces and frictional resistive forces compete (middle). The blue arrows report the average fluid velocity induced by the cell, defined as the flow rate divided by the cross-sectional area of the capillary. The surface of the idealized model is decorated along slip lines by material particles to highlight their motion relative to the capillary walls in the contact region.

Supplementary Movie S10: Video recordings of an *Euglena* cell effectively crawling by metaboly (right) in the presence of a immobile cell, stuck in the capillary and acting as a hydraulic plug (left).

Supplementary Movie S11: Video recordings of *Euglena gracilis* performing metaboly in a capillary and of suspended polystyrene beads by combining brightfield and fluorescence microscopy. Data from these experiments allowed us to quantify the fluid flow around crawling cells by tracking the fluorescent beads. Only beads in the vicinity of the cell undergo rapid motions due to local flows induced by shape changes and flagellar beating.

Supplementary Movie S12: *Euglena gracilis* crawling by metaboly while confined into a glass capillary. Observation using brightfield reflected light microscopy allows for the visualization of the pellicle strips in contact with the capillary wall. The microscope was intermittently focused at the pellicle-capillary interface to visualize the pellicle and at the capillary axis to visualize cell shape. The movie reports also the kymograph relative to the capillary axis. The trajectories of pellicle features reveal sliding between the pellicle and the capillary wall in the contact region.

Supplementary Movie S13: Computational results from the theoretical model of crawling by metaboly under confinement. Results are shown for increasing confinement, as quantified by ratio of $d_{\mathrm{cap}}/d_{\mathrm{cell}} = \{0.875, 1.0, 1.375, 1.8\}$, in the limit of high hydraulic resistance, and during three cycles. The cell motion

16

is reported by black and white features fixed in the frame of the capillary. Notice that the model self-adapts to imposed confinement by developing a limit cycle (gait), which is consistent with the experimental observations on *Euglena* cells. The four gaits at different degrees of confinement are the result on the same activation pattern, represented as a space-time colormap (left).

Supplementary Movie S14: Video recordings of *Distigma proteus* between glass slides separated on one side by a spacer of thickness $\sim 80\,\mu m$ in order to realize a wedge-shaped fluid chamber. In the absence of confinement (gap between plates $\sim 36\,\mu m$), cells exhibit flagellar swimming. Significant confinement between the two plates (gap $\sim 5\,\mu m$) triggers non-reciprocal peristaltic cell deformations, which allow *Distigma* cells to crawl.

Supplementary Movie S15: Video recordings of *Peranema trichophorum* between glass slides separated on one side by a spacer of thickness $\sim 80\,\mu m$ in order to realize a wedge-shaped fluid chamber. In the absence of confinement (gap between plates $\sim 52\text{-}43\,\mu m$), cells glide on the substrate thanks to the movement of their flagellum. During gliding, cells occasionally bend their body, and this shape change is associated with sharp turns of the cell trajectory. Under high confinement between the glass plates (gap $\sim 7\,\mu m$), cells are not able to glide and develop periodic, largely reciprocal shape changes.

Supplementary References

[36] do Carmo, M. P. *Differential geometry of curves and surfaces*. Prentice-Hall, Englewood Cliffs (1976).

[37] Klein, J. Hydration lubrication. *Friction* **1,** 1-23 (2013).

[38] Kim, S. & Karrila, S. J. *Microhydrodynamics: Principles and Selected Applications*. Courier Corporation, Mineola (2013).

[39] Doi, M. Onsager's variational principle in soft matter. *J. Phys.: Condens. Matter* **23,** 284118 (2011).

[40] Arroyo, M., Walani, N., Torres-Sánchez, A. & Kaurin, D. Onsager's variational principle in soft matter: Introduction and application to the dynamics of adsorption of proteins onto fluid membranes. In: Steigmann, D. J. (ed) *The Role of Mechanics in the Study of Lipid Bilayers* Springer International Publishing, Cham (2018).

[41] Saito, A. et al. Gliding movement in *Peranema trichophorum* is powered by flagellar surface motility. *Cell Motil. Cytoskeleton* **55,** 244-253 (2003).

[42] Chang, S. L. Observations on the organelles, movement, and feeding of *Peranema trichophorum* (Ehrb.) Stein. *T. Am. Microsc. Soc.* **85,** 29-45 (1966).